

# Mr. Tompkins world: Effects of extreme variations in fundamental constants on the structure of atoms, molecules, and periodic table

Vsevolod D. Dergachev,<sup>1</sup> Hoang Bao Tran Tan,<sup>2</sup> Sergey A. Varganov,<sup>1,\*</sup> and Andrei Derevianko<sup>2,†</sup>

<sup>1</sup>*Department of Chemistry, University of Nevada, Reno, Nevada 89557, USA*

<sup>2</sup>*Department of Physics, University of Nevada, Reno, Nevada 89557, USA*

(Dated: February 10, 2022)

In 1939, George Gamow published the book “Mr. Tompkins in Wonderland”, which tells a story about a world where fundamental constants have radically different values from those they have in the real world. Gamow’s classic predates modern theories that generically promote fundamental constants to dynamic entities. Constants are no longer constant. Enter Mr. Tompkins world where the speed of light  $c$  is reduced to that of a speeding bicycle. Here we show that reducing  $c$  from its nominal value truncates periodic system of elements, qualitatively changes the aufbau principle in atoms, and modifies the nature of chemical bond and the structure of molecules. Noble gasses are no longer inert. Water fails to serve as a universal solvent. In addition to pushing relativistic quantum chemistry to its limits, our analysis lends further support to the anthropic principle: life as we know it can happen only in a certain range of fundamental constants.

Quantum chemistry primarily depends on a set of three fundamental constants (FCs): the electron mass  $m_e$ , the elementary charge  $e$ , and the Planck constant  $\hbar$ . Relativity brings in the speed of light  $c$  or, equivalently, the fine-structure constant  $\alpha = e^2/\hbar c$ . These constants, together with the nuclear parameters, are fixed in conventional computations to their empirical or nominal values. Modern theories, however, generically promote FCs to dynamic entities [1, 2]. Constants are no longer constant. Previous literature on variations of FCs predominantly focused on small deviations from their nominal values [3–5]. In this paper, we explore a novel regime of *extreme* variations that are motivated by dark matter models [6]. We find an abundance of remarkable effects on the structure of atoms and molecules and, by extension, on the fundamental conditions for the emergence and sustainability of life, i.e., the so-called anthropic principle in cosmology [7, 8].

The variation of FCs in the non-relativistic Born-Oppenheimer (NR-BO) approximation reduces to the isotropic scaling of all nuclear and electronic coordinates by the Bohr radius  $a = \hbar^2/m_e e^2$ , see Appendix A. As a result, molecular bond angles do not depend on FCs. Similarly, all the FC-dependence of energies factorizes out via the Hartree energy  $m_e e^4/\hbar^2$ . Effects beyond the NR-BO approximation violate these scaling laws and lead to changes in bond angles with varying FCs. For concreteness, here we focus on the role of relativity and examine the consequence of varying  $\alpha$ . In atomic units ( $m_e = |e| = \hbar = 1$ ),  $\alpha = 1/c$  and variations in  $\alpha$  are equivalent to those in  $c$  via  $c/c_0 = \alpha_0/\alpha$ . Here and below, the subscript 0 of a quantity refers to its nominal value, e.g.,  $\alpha_0 \approx 1/137$ .

Beyond connections to novel theories, there is a practical utility in artificially enhancing relativity [9]. Be-

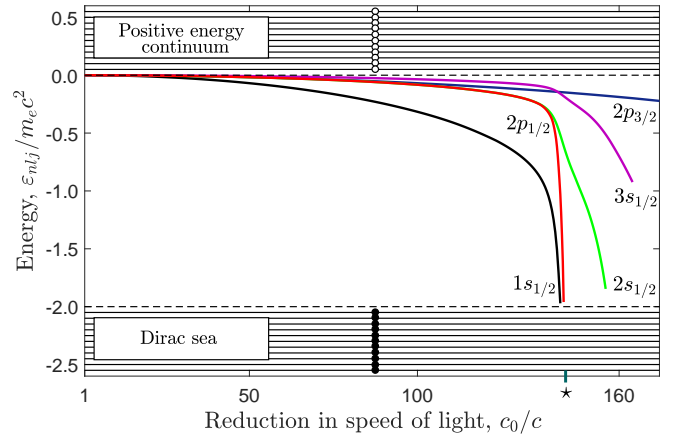


FIG. 1. Energy levels of atomic hydrogen as a function of speed of light, based on solving the Dirac equation with finite-sized proton. The  $1s_{1/2}$  level “dives” into the Dirac sea at the critical value  $c^* \approx c_0/143$ .

cause an electron near the nucleus of charge  $Z$  moves with speed  $v/c \sim \alpha Z$ , relativistic effects are most pronounced in heavy systems. However, in heavy atoms and molecules, the role of relativity are often masked by large electron correlations. Reducing  $c$  magnifies the role of relativity in molecules comprising *light* atoms, where correlations can be treated with much higher accuracy. It is worth emphasizing that for small speeds of light,  $v/c \sim 1$ , and one must solve the non-perturbative four-component Dirac equation [10, 11]. We carry out *ab initio* relativistic quantum chemistry calculations with the state-of-the-art DIRAC package [12, 13], exploring its capabilities in the ultra-relativistic regime.

We start with a hydrogen atom. Its ground state energy is given by [14]

$$\varepsilon_{1s_{1/2}} = c^2 \left( \sqrt{1 - (Z/c)^2} - 1 \right). \quad (1)$$

We remind the reader that the Dirac equation has two

\* Corresponding author; [svarganov@unr.edu](mailto:svarganov@unr.edu)

† Corresponding author; [andrei@unr.edu](mailto:andrei@unr.edu)



is expected to have as rich a chemistry as carbon, e.g., it may engender an ultra-relativistic version of organic chemistry. It is intriguing to imagine polymers, nanostructures, and an entirely new biology where neon plays the traditional role of carbon.

Our calculations for second-period atoms with electrons in the  $2p_{3/2}$  shell (N, O, F, and Ne) demonstrate similar non-trivial changes in the nature of their ground states near their respective  $c^*$  (see Appendix C), consistent with the modified aufbau principle of Fig. 2. Qualitatively, the  $2p_{3/2}$  orbital dives into the Dirac sea at  $c$  substantially lower than that for  $2p_{1/2}$ , see Fig. 1. This leads to a giant  $\sim m_e c^2$  fine-structure splitting near the critical value  $c^*$ . For the same reason, there is a large difference in the relativistic contraction of the  $2p_{3/2}$  and  $2p_{1/2}$  orbitals near  $c^*$ : the  $2p_{1/2}$  (and the  $3s_{1/2}$ ) shells become submerged inside the  $2p_{3/2}$  shell. This drives a more effective screening of the nuclear charge by the inner shells causing an increase in our computed  $2p_{3/2}$  orbital energies with decreasing  $c$  in many-electron atoms — a trend opposite to that in the H-like ions, Fig. 1. These effects also lead to dramatic changes in the geometry of molecules containing these atoms.

How would the extreme variation of the speed of light affect the structure and properties of molecules? Here we address this question by focusing on water and ammonia. All known forms of life use water as a universal solvent for various chemicals and as an essential component of many metabolic processes [20]. Ammonia is an important source of nitrogen required for the synthesis of amino acids, for building proteins in living systems [21], and as an alternative universal solvent [20].

The formation of molecular orbitals (MOs) from atomic orbitals requires energy resonances and overlaps between the constituent atomic orbitals. Relativity affects the resonances via the different rates of stabilization of energies and the overlaps via the varying degrees of contraction of atomic orbitals. When the speed of light is reduced, the geometry of the water molecule changes, with the initial contraction of the bond angle and the subsequent complete straightening of the molecule, Fig. 4. We find that at  $c \approx c_0/14$ , the calculated bond angle in water decreases from the nominal  $104.5^\circ$  to  $90^\circ$ . At  $c \approx c_0/18$ , the water molecule becomes linear and therefore nonpolar. These dramatic changes in the molecular geometry are induced by the relativistic stabilization of the  $2s_{1/2}$  and  $3s_{1/2}$  orbitals with respect to the  $2p_j$  orbitals of the oxygen atom, and by the increased fine-structure splitting between the  $2p_{1/2}$  and  $2p_{3/2}$  orbitals, Fig. 4. These effects drive changes in the molecular geometry which can be understood using the valence-shell electron-pair repulsion (VSEPR) and the MO models [22].

According to the VSEPR model, at the nominal  $c$ , the valence  $2s$  and the three valence  $2p$  atomic orbitals of oxygen mix to form four equivalent hybrid orbitals ( $sp^3$  hybridization, or  $2s_{1/2}2p_{1/2}2p_{3/2}$  in relativistic notation). Two of the hybrid orbitals overlap with the hydrogen  $1s$

orbitals, and the remaining two hold the two lone electron pairs. The repulsion between the four electron pairs on the hybrid orbitals leads to the slightly distorted tetrahedral arrangement, corresponding to the bond angle of  $104.5^\circ$ .

At the intermediate  $c \approx c_0/14$ , the stabilization of the  $2s_{1/2}$  and  $2p_{1/2}$  orbitals in oxygen breaks down the  $sp^3$  hybridization. This results in an energetically isolated  $2p_{3/2}$  orbital, which can accommodate up to four electrons forming the oxygen-hydrogen bonds. This stabilizes the molecular structure, resulting in an  $90^\circ$  bond angle [9]. The stabilization of the  $2s_{1/2}$  and  $2p_{1/2}$  atomic orbitals also drives changes in the distributions of the electron radial density in  $\text{H}_2\text{O}$ , see Fig. 14. The computed radial density distributions reduce to those of the  $2s_{1/2}$  and  $2p_{1/2}$  atomic orbitals, which no longer participate in chemical bonding.

At even smaller  $c \approx c_0/18$ , the lowering of the  $3s_{1/2}$  energy and the raising of the  $2p_{3/2}$  energy in oxygen leads to these two orbitals becoming quasi-degenerate. This induces the  $ps$  hybridization between the half-filled  $2p_{3/2}$  and the  $3s_{1/2}$  shells [9], resulting in the linear molecular geometry. The participation of the  $3s_{1/2}$  orbital in the chemical bonding is supported by our calculated radial density distribution for the HOMO-1 (HOMO is the highest occupied MO) of water: near  $c^*$ , the shape of this distribution closely resembles that of the  $3s_{1/2}$  atomic orbital, see Fig. 14.

The Walsh correlation diagrams of the MO theory provide more insights into the relation between the electronic structure and geometry of the water molecule, see Fig. 5. These diagrams show the energies of valence MOs as functions of the bond angle. Because the total energy of a molecule can be approximated as the sum of MO energies, the Walsh diagrams can be used to predict the values of the bond angle that minimize the total energy. At  $c = c_0$ , the interplay between the HOMO-1 and HOMO-2 energies minimizes the total energy at the bond angle of  $104.5^\circ$ . As the speed of light decreases, the  $2s_{1/2}$  orbital stabilizes and its contribution to HOMO is diminished, leading to the minima of the HOMO and total energies at the  $90^\circ$  bond angle. At even lower speed of light, the relativistically stabilized  $3s_{1/2}$  orbital starts to contribute to HOMO, leading to the linear geometry.

The modifications of the molecular geometry of ammonia at reduced speeds of light resemble those of water and can be similarly explained by the changes in the electronic structure of the nitrogen and oxygen atoms, see Figs. 10, 11. At the nominal speed of light, the VSEPR model predicts the formation of four equivalent  $sp^3$  hybrid orbitals in nitrogen, forming a tetrahedral arrangement. Three of these hybrid orbitals form chemical bonds with the hydrogen atoms, while the fourth orbital holds the lone electron pair, leading to the trigonal pyramidal geometry, with the bond angle of  $106.8^\circ$ , see Fig. 6.

As  $c$  decreases, the  $\text{NH}_3$  molecule becomes first more pyramidal, but then completely flattens. At  $c \approx c_0/18$ , the  $\text{NH}_3$  bond angle reduces to its minimum value of  $87^\circ$ .

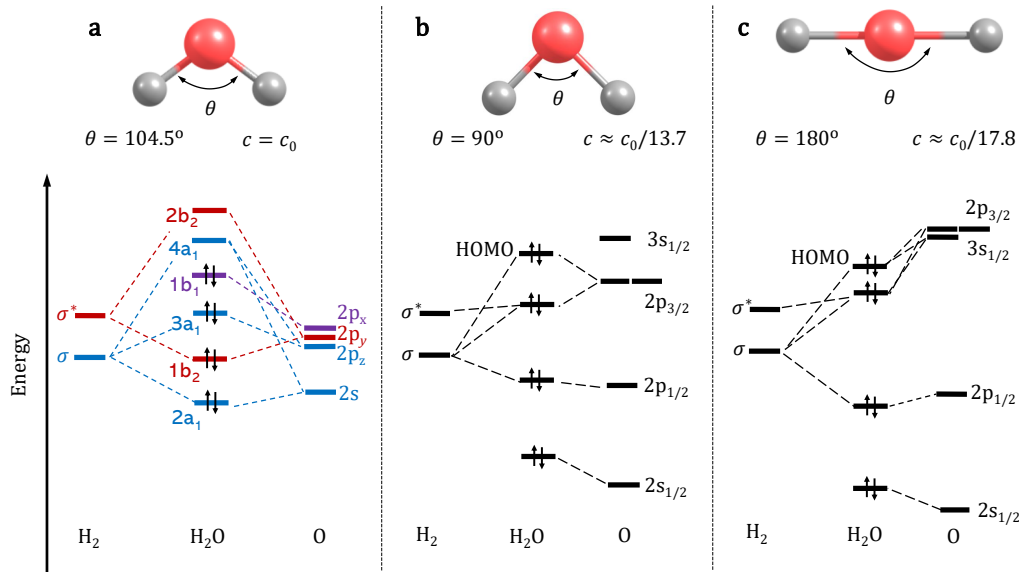


FIG. 4. Molecular geometry and orbital diagram of water at different speeds of light, (a)  $c = c_0$ , (b)  $c \approx c_0/13.7$ , and (c)  $c \approx c_0/17.8$ . At the nominal speed of light (panel a), the orbitals are labeled and coloured according to their irreducible representations in the  $C_{2v}$  point group. At the decreased speeds of light (panels b and c), only the occupied molecular orbitals are shown.

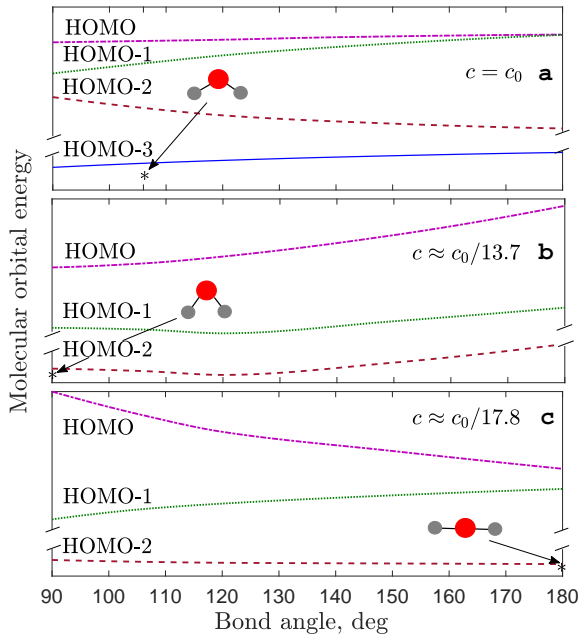


FIG. 5. Walsh correlation diagrams of water showing the energies of four valence molecular orbitals as functions of the bond angle at different speeds of light, (a)  $c = c_0$ , (b)  $c \approx c_0/13.7$ , and (c)  $c \approx c_0/17.8$ . In panels b and c, the lowest occupied molecular orbital is omitted as it reduces to the  $2s_{1/2}$  atomic orbital of oxygen and does not participate in the formation of oxygen-hydrogen bonds. The arrows indicate the bond angle at which the molecular geometry stabilizes. The energies of molecular orbitals at the equilibrium bond angles correspond to those in Fig. 4.

This can be explained by the loss of the hybridization due to the relativistic stabilization of the  $2s_{1/2}$  atomic orbital of nitrogen. A  $\sim 20$ -fold decrease in the speed of light leads to the planar geometry with a  $120^\circ$  bond angle. This is due to the induced quasi-degeneracy between the  $2p_{3/2}$  and  $3s_{1/2}$  orbitals, which leads to the formation of the  $p^2s$  hybrid orbitals. These observations are further supported by the calculated radial density distributions of the occupied MOs in ammonia, see Fig. 16.

The striking changes in the geometries of the oxygen and nitrogen-containing molecules at reduced speeds of light would lead to alternative chemistry and biology. For example, in contrast to the bent water molecules that form three-dimensional networks of hydrogen bonds, the ultra-relativistic linear water molecules could only form two-dimensional networks. This is anticipated to substantially decrease the freezing and boiling points of water [23, 24]. In addition, the linear water molecule would have no dipole moment. Thereby, water would cease to serve as a universal solvent. Clearly, life as we know it can only happen in a certain range of values of fundamental constants (the anthropic principle [7, 8]).

However, the anthropic principle constraints on the variation of FCs can be evaded for certain clumpy dark matter models [6]. In these models, the FCs inside and outside the dark matter clumps can differ substantially. Encounters of the solar system with dark matter clumps can be exceedingly rare, while the laboratory searches [25] so far only extend over a cosmologically short 20-year recent history. Our predicted changes in the geometry of ammonia, one of the most abundant polyatomic molecules in the interstellar space [26], can be potentially used in astrophysical searches for such “Mr.

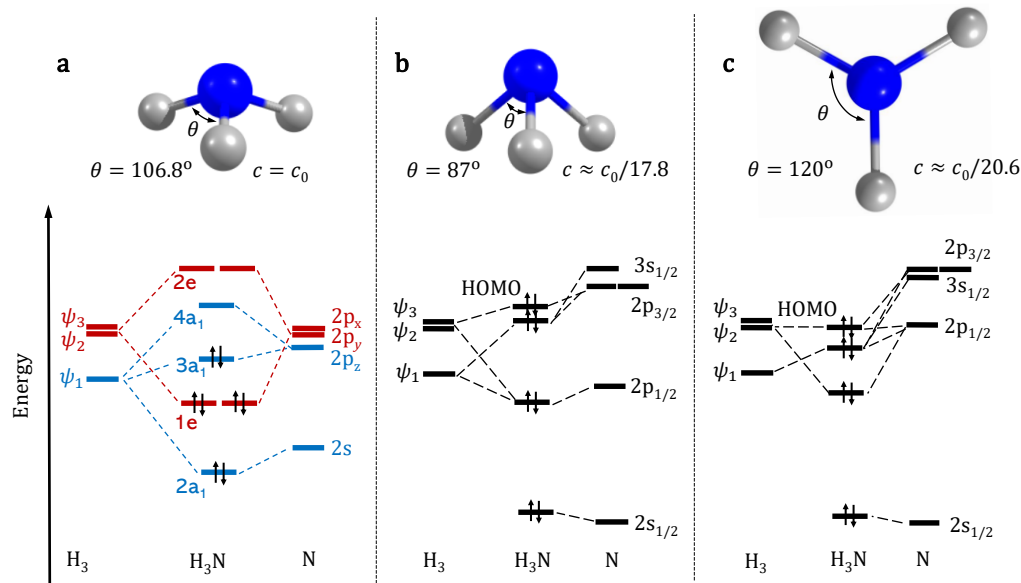


FIG. 6. Molecular geometry and orbital diagram of ammonia at different speeds of light, (a)  $c = c_0$ , (b)  $c \approx c_0/17.8$ , and (c)  $c \approx c_0/20.6$ . At the nominal speed of light (panel a), the orbitals are labeled and coloured according to their irreducible representations in the  $C_{3v}$  point group. At decreased speed of light (panels b and c), the spin-orbital notation is used for atomic nitrogen, and only the occupied molecular orbitals are shown.

Tompkins” clumps: as a clump sweeps through an interstellar cloud, for example, it would induce observable changes in properties of the molecules comprising the cloud.

## METHODS

The critical values of the speed of light for the hydrogen atom and hydrogen-like ions were calculated by solving the Dirac equation with the finite nucleus models using both analytical and numerical methods, as described in Appendix B. For many-electron atoms, the four-component Dirac equation was solved using the Kramer Restricted Configuration Interaction (KRCI) method, as implemented in the DIRAC19 package [13]. The reference wavefunctions for the KRCI calculations were obtained by solving the average-of-configuration open-shell Dirac-Hartree-Fock (DHF) equation. In the atomic DHF calculations, all configurations generated by distributing the valence electrons over the  $2s$ ,  $2p$  and  $3s$  orbitals were included. To accurately describe electron density near nuclei at the slower speeds of light, the original aug-cc-pV6Z basis set was augmented with large-exponent  $s$  and  $p$  functions, see Appendix C for more details. The molecular geometries of water and ammonia were optimized using the closed-shell DHF method with the same basis set. Neglecting the effects of electron correlation in molecular calculations resulted in the deviation of the water and ammonia bond angles from their experimental values by less than 2%, which is sufficiently accurate for our purpose.

## ACKNOWLEDGMENTS

We thank Mikhail Kozlov and Xiaoyong Chu for discussions. This work was supported in part by the U.S. National Science Foundation under Grants PHY-1912465 and CHE-1654547, and by the Sara Louise Hartman endowed professorship in Physics.

### Appendix A: Invariance of molecular geometry under variation of fundamental constants in the non-relativistic Born-Oppenheimer approximation

The goal of this section is to prove that the variation of fundamental constants cause all the molecular bonds to stretch/dilate by the very same scaling factor, leaving the angles between molecular bonds unaffected, see Fig. 7. This statement holds only with the assumption of (i) the non-relativistic approximation, (ii) infinitely-heavy nuclei (Born-Oppenheimer approximation) and, (iii) point-like spinless nuclei. If any one of these assumptions is violated, molecular bond angles would vary with changing FCs.

We begin by considering an arbitrary molecule containing  $N_n$  point-like nuclei and  $N_e$  electrons. Under the enumerated assumptions, the non-relativistic Born-

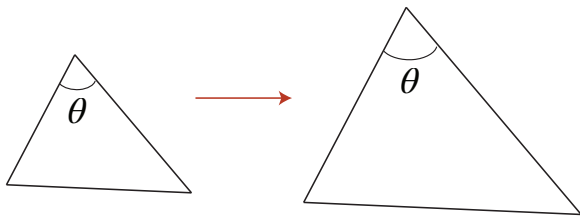


FIG. 7. Scaling all the sides of the triangle by the same numerical factor does not affect the value of angle  $\theta$  (or of any other angle in the triangle). This example can be generalized to 3D geometry: angles and thus the molecular geometry are not affected by scaling of all the inter-nuclear distances by the same factor (isotropic scaling transformation).

Oppenheimer (NR-BO) Hamiltonian has the form

$$H_{\text{NR-BO}} = \sum_i -\frac{\hbar^2}{2m_e} \Delta_{\mathbf{r}_i} + \frac{1}{2} \sum_{i \neq j} \frac{e^2}{|\mathbf{r}_i - \mathbf{r}_j|} \quad (\text{A1})$$

$$+ \frac{1}{2} \sum_{n \neq n'} \frac{Z_n Z_{n'} e^2}{|\mathbf{R}_n - \mathbf{R}_{n'}|} - \sum_{i,n} \frac{Z_n e^2}{|\mathbf{R}_n - \mathbf{r}_i|}.$$

Here, for clarity, we retained all the fundamental constants (FCs) and we use the Gaussian system of electromagnetic units. We labeled the positions of electrons as  $\mathbf{r}_i$  and those of nuclei as  $\mathbf{R}_n$ , with  $Z_n$  being nuclear charges. All the terms in  $H_{\text{NR-BO}}$  have their usual meaning: the kinetic energy of electrons, the electron repulsion, the nuclear repulsion, and the electron-nucleus attraction, respectively. The assumption of infinitely heavy nuclei allows the nuclear kinetic terms to be neglected.

To determine the molecular geometry in the BO approximation, one first solves the time-independent Schrödinger equation the positions of the nuclei fixed,

$$H_{\text{NR-BO}}(\mathbf{r}_e | \mathbf{R}_n) \Psi(\mathbf{r}_e | \mathbf{R}_n) = E(\mathbf{R}_n) \Psi(\mathbf{r}_e | \mathbf{R}_n). \quad (\text{A2})$$

Here the Hamiltonian  $H$  and thus the eigenfunctions  $\Psi$  and energies  $E$  depend on fundamental constants:  $E(\mathbf{R}_n | m_e, \hbar, e)$ . After the potential surfaces  $E(\mathbf{R}_n | m_e, \hbar, e)$  are obtained as functions of nuclear coordinates, the equilibrium nuclear positions,  $\{\mathbf{R}_n^{\text{eq}}\}$ , are determined by minimizing the energy

$$\min_{\{\mathbf{R}_n\}} E(\mathbf{R}_n | m_e, \hbar, e) \Rightarrow \{\mathbf{R}_n^{\text{eq}}\}. \quad (\text{A3})$$

We would like to explicitly factor out the dependence on FCs from Eq. (A2). To this end, we rescale all the coordinates by the same factor  $\xi$ :  $\mathbf{r}_i \rightarrow \xi \boldsymbol{\rho}_i$ ,  $\mathbf{R}_n \rightarrow \xi \boldsymbol{\rho}_n$ . Upon substitution into  $H_{\text{NR-BO}}$ , the kinetic energy term is transformed into  $-\sum_i^{N_e} \hbar^2 \Delta_{\boldsymbol{\rho}_i} / (2m_e \xi^2)$  and all the electro-static interaction potentials are divided by  $\xi$ . We may choose  $\xi$  so that the dimensionful prefactors in the kinetic and potential energy contributions equal one another, i.e.,

$$\frac{\hbar^2}{m_e \xi^2} = \frac{e^2}{\xi}. \quad (\text{A4})$$

This particular choice of  $\xi$  enables us to factor out the dependence on the FCs from the Hamiltonian  $H_{\text{NR-BO}}$ . Solving Eq. (A4) results in

$$\xi = \frac{\hbar^2}{m_e e^2} = a, \quad (\text{A5})$$

where  $a$  is the Bohr radius.

With this choice, the Hamiltonian admits the factorization  $H_{\text{NR-BO}} = E_h h(\boldsymbol{\rho}_e | \boldsymbol{\rho}_n)$ , where

$$E_h = \hbar^2 / m_e \xi^2 = e^2 / \xi = m_e e^4 / \hbar^2 \quad (\text{A6})$$

is the atomic unit of energy (Hartree) and  $h(\boldsymbol{\rho}_e | \boldsymbol{\rho}_n)$  is a scaled Hamiltonian which does not depend on FCs. The solution of the eigenvalue equation

$$h(\boldsymbol{\rho}_e | \boldsymbol{\rho}_n) \varphi(\boldsymbol{\rho}_e | \boldsymbol{\rho}_n) = \varepsilon(\boldsymbol{\rho}_n) \varphi(\boldsymbol{\rho}_e | \boldsymbol{\rho}_n). \quad (\text{A7})$$

which is the rescaled version of Eq. (A2), does not depend on FCs either. The full energy  $E(\mathbf{R}_n)$  is obtained from  $\varepsilon(\boldsymbol{\rho}_n)$  via

$$E(\mathbf{R}_n | m_e, \hbar, e) = \frac{m_e e^4}{\hbar^2} \varepsilon(\boldsymbol{\rho}_n),$$

which shows that the minimum of  $E(\mathbf{R}_n | m_e, \hbar, e)$  is attained at the point

$$\mathbf{R}_n^{\text{eq}} = \frac{\hbar^2}{m_e e^2} \boldsymbol{\rho}_n^{\text{eq}}, \quad (\text{A8})$$

where  $\boldsymbol{\rho}_n^{\text{eq}}$  is obtained by finding the equilibrium positions

$$\min_{\{\boldsymbol{\rho}_n\}} \varepsilon(\boldsymbol{\rho}_n) \Rightarrow \{\boldsymbol{\rho}_n^{\text{eq}}\}, \quad (\text{A9})$$

and is thus FC-independent.

To reiterate, in the non-relativistic Born-Oppenheimer approximation, as the FCs are varied from their nominal values, all the equilibrium positions are scaled by the very same factor,

$$\mathbf{R}_n^{\text{eq}} = \frac{a}{a_0} \mathbf{R}_{n,0}^{\text{eq}}. \quad (\text{A10})$$

Here and below all the quantities with the subscript 0 refer to the nominal values. Equation (A10) represents an isotropic scaling of all the coordinates by the same factor, leaving all molecular bond angles unaffected, see Fig. 7.

The fact that the isotropic scaling does not affect angles in a molecule of arbitrary geometry can be formally proven as follows. Choose  $\{\mathbf{R}_n\}_{n=1, \dots, N}$  to be (equilibrium) position vectors of all  $N$  nuclei in a molecule. The angle  $\theta_{ab}$  between a pair of these vectors,  $\mathbf{R}_a$  and  $\mathbf{R}_b$ , is given by

$$\theta_{ab} = \cos^{-1} \left[ \frac{(\mathbf{R}_a \cdot \mathbf{R}_b)}{|\mathbf{R}_a| |\mathbf{R}_b|} \right], \quad (\text{A11})$$

where we used the conventional definition of scalar products and  $|\mathbf{R}_n| = \sqrt{(\mathbf{R}_n \cdot \mathbf{R}_n)}$  is the length of the vector.

Should all the position vectors be scaled by some factor  $\lambda$ ,  $\mathbf{R}_n \rightarrow \lambda \mathbf{R}_n$ , the factors of  $\lambda$  in Eq. (A11) cancel out. Thereby, the angles between molecular bonds are not affected by the isotropic scaling. The entire molecule undergoes isotropic stretching or dilation as the FCs are varied.

In addition, as follows from our derivation, all the electron coordinates undergo the same isotropic scaling,

$$\mathbf{r}_e = \frac{a}{a_0} \mathbf{r}_{e,0}. \quad (\text{A12})$$

In particular, this means that the sizes of electronic clouds and atoms are scaled by the same  $a/a_0$  ratio. Another point is that all the energies (both atomic and molecular) are scaled by the atomic unit of energy

$$E = \frac{E_h}{E_{h,0}} E_0. \quad (\text{A13})$$

These observations offer a visualization: as a ‘‘Mr. Tompkins’’ clump, introduced in the main text, sweeps through an atom or a molecule, all the energy levels are gently modulated and the atom or molecule ‘‘breathes’’ in accordance with the local values of FCs. This picture is valid in the regime of sufficiently large and slow clumps. The clumps need to be sufficiently large, so that there are no gradients of FCs across the extent of the individual atom or molecule. The clumps have to be sufficiently slow, so that the induced perturbation does not cause transitions between molecular or atomic levels. Then the atom or molecule follows the change in FCs adiabatically.

It is worth emphasizing that our proof heavily relies on the possibility of factoring out all the dependence on FCs in various contributions to the  $H_{\text{NR-BO}}$  Hamiltonian. If we were to add kinetic energies of the nuclei to  $H_{\text{NR-BO}}$ , our coordinate scaling procedure would result in the requirement

$$\frac{\hbar^2}{m_e \xi^2} = \frac{e^2}{\xi} = \frac{\hbar^2}{M_1 \xi^2} = \dots = \frac{\hbar^2}{M_N \xi^2}, \quad (\text{A14})$$

where  $M_n$  are the nuclear masses. Generically, these equalities can not be satisfied simultaneously by any choice of the scaling parameter  $\xi$ .

Our factorization procedure depends on the fact that the Coulomb interactions in the  $H_{\text{NR-BO}}$  Hamiltonian exhibited power-law dependence with respect to distances. If the nuclei have finite size, the Hamiltonian no longer admits simple coordinate scaling. Moreover, introducing nuclear properties (such as finite-size charge distribution or hyperfine interactions with nuclear moments) into the problem brings in another FC,  $m_q/\Lambda_{\text{QCD}}$ , where  $m_q$  is the average mass of up and down quarks and  $\Lambda_{\text{QCD}}$  is the energy scale of quantum chromo-dynamics.

Similarly, the Dirac equation does not admit factoring out all the FCs in the Hamiltonian. Indeed, even in the simplest case of the hydrogen atom with an infinitely-heavy point-like nucleus, the Dirac Hamiltonian contains

three terms,

$$h_{\text{D}} = -i\hbar c \boldsymbol{\alpha} \cdot \boldsymbol{\nabla} + \beta m_e c^2 - \frac{e^2}{r}. \quad (\text{A15})$$

Since the  $4 \times 4$  Dirac matrices  $\boldsymbol{\alpha}$  and  $\beta$  are collections of FC-independent c-numbers, our coordinate scaling procedure results in the requirement

$$\frac{\hbar c}{\xi} = m_e c^2 = \frac{e^2}{\xi}. \quad (\text{A16})$$

For arbitrary values of FCs ( $m_e$ ,  $\hbar$ ,  $e$ , and  $c$ ), these equalities cannot be simultaneously satisfied. We conclude that relativity must lead to the breakdown of the isotropic scaling of atomic structure and molecular geometry with varying FCs. Molecular bond angles vary with changing FCs due to relativistic effects.

Since the theory of quantum electrodynamics (QED) is built on the quantization of relativistic fields, field-theoretic effects also lead to the breakdown of the isotropic scaling with varying FCs. This can be easily understood by examining the effects of vacuum polarization by the nucleus [16]. In QED, a nucleus is immersed into a nuclear-field-polarized cloud of virtual pairs of particles and anti-particles. Vacuum polarization leads to the replacement of the pure Coulomb potential  $-Z/r$  of a point-like nucleus by the Uehling potential. The success of our factorization procedure depends on the fact that the Coulomb interactions in the NR-BO Hamiltonian exhibits a power-law dependence with respect to distances. The Uehling potential lacks this power-law dependence and, thereby, does not admit factoring out FCs in the resulting Hamiltonian.

To recapitulate, the isotropic scaling of molecular geometry preserves angles between molecular bonds in the NR-BO approximation. Molecules ‘‘breathe’’ with varying FCs.

Finally, consider a thought experiment where we compare lengths of two rulers of different chemical composition. Suppose at the nominal values of FCs both rulers have the same lengths. As the FCs change, both rulers are expanding/contracting by the same factor in the NR-BO approximation. The observer would not be able to tell if FCs have changed. The very same argument applies to transition frequency comparisons: in the NR-BO approximation, all the dependence of electronic energies on FCs is governed by the common factor of Hartree energy  $m_e e^4/\hbar^2$ . Corrections to the most basic NR-BO approximation violate this isotropic scaling law: the lengths of two rulers in our thought experiment would differ for varying FCs. Similarly, the ratios of transition frequencies for two different atoms or molecules would change with varying FCs.

## Appendix B: Critical values of $\alpha$

As discussed in the main text, the well-known analytical solution of the Dirac equation for hydrogen-like ions

with a point-like nucleus is inadequate for determining the critical values  $\alpha^*$  of the electromagnetic fine-structure constant. In this section, we solve this problem using the more realistic finite-sized nucleus model. We also discuss the critical values of  $\alpha$  for multi-electron atoms and the truncation of periodic system at reduced speed of light.

The critical value  $\alpha^*$ , specific to an atomic energy level, is determined by the requirement that the energy  $\varepsilon$  of that level becomes equal to the Dirac sea threshold,  $\varepsilon = -2m_e c^2$  (see the main text). Here and below the rest mass energy  $m_e c^2$  is excluded from  $\varepsilon$ . For some simple models of the nuclear charge density, this problem can be solved analytically by generalizing the solution for a similar problem of determining the critical nuclear charge for the fixed nominal value of  $\alpha$  (see, for example, Refs. [15, 16]).

The analytical solution can be developed for a spherical shell-like nuclear charge density distribution,  $\rho_{\text{shell}}(r) \propto \delta(r - R)$ , where  $R$  is the radius of the nuclear charge shell. Inside the nuclear shell,  $r < R$ , the potential is constant  $V(r) = -Ze^2/R$  and the solution to the Dirac equation is given by the free particle solution regular at the origin. Outside the nuclear shell, the potential is of a pure Coulomb character,  $V(r) = -Ze^2/r$ , and the solution to the Dirac equation is a linear combination of the regular and irregular relativistic Coulomb wavefunctions. Setting  $\varepsilon = -2m_e c^2$  and matching the inner and outer solutions at  $r = R$ , we find, for the  $ns_{1/2}$  orbitals, the following transcendental equation for  $\alpha^*$

$$\xi \frac{K'_{i\nu}(\xi)}{K_{i\nu}(\xi)} = 2(\alpha^* Z) \cot(\alpha^* Z), \quad (\text{B1})$$

where  $\xi = \sqrt{8ZR/a_0}$ ,  $K_{i\nu}(\xi)$  is the modified Bessel function of the second kind (also known as the Macdonald function) with index  $\nu \equiv 2\sqrt{(\alpha^* Z)^2 - 1}$ .  $K'_{i\nu}(\xi)$  is the derivative of  $K_{i\nu}(\xi)$  with respect to  $\xi$ . Equation (B1) has infinitely many roots, which correspond to increasing values of the principal quantum number  $n$ . The lowest value of the root determines  $\alpha^*$  for the  $1s_{1/2}$  orbital.

To solve Eq. (B1), we need to specify the nuclear charge shell radius  $R$ . We make a connection to the more realistic nuclear charge distributions by noticing that for the spherical shell distribution, the root-mean-square (rms) radius  $R_{\text{rms}}$  is identical to  $R$ . For proton, we take the 2018 CODATA [27] recommended value,  $R_{\text{rms}}(^1\text{H}) = 0.8414(19)$  fm. For heavier elements, we use an approximation [16]  $R \approx 1.6 Z^{1/3}$  fm, adequate for our semi-qualitative discussions. From Eq. (B1) we find the critical value of  $\alpha$  for hydrogen  $1s_{1/2}$  to be  $\alpha^* \approx 1.04$  or, equivalently,  $c^* \approx c_0/143$ .

One may argue that the spherical shell approximation for the nuclear charge distributions used in deriving Eq. (B1) is not realistic. To address this question, we solved the Dirac equation for hydrogen numerically using the finite-difference techniques [28]; for a uniform nuclear charge distribution we find  $\alpha^* \approx 1.042$ . This is to be compared to the spherical shell result of 1.040. A similar exercise for fermium ( $Z = 100$ ,  $A = 257$ ,  $R_{\text{rms}} = 7.1717$  fm)

shows that the  $1s_{1/2}$  value of  $\alpha^*$  is  $1.20 \times 10^{-2}$  for the spherical shell distribution and  $1.18 \times 10^{-2}$  for both the uniform and the Fermi nuclear charge distributions. Thus the accuracy of the spherical shell approximation for the nuclear charge distribution is  $\sim 0.1 - 1\%$ , which is adequate for our goals.

We note that the DIRAC19 package internally uses the Gaussian nuclear charge distributions with  $R_{\text{rms}}$  given by the fitting formula [29]

$$R_{\text{rms}} = 0.836 A^{1/3} + 0.570 (\pm 0.05) \text{ fm}. \quad (\text{B2})$$

For a given charge  $Z$  we use the mass number  $A$  for the most abundant isotope. This formula results in the proton  $R_{\text{rms}}(^1\text{H}) = 1.406$  fm which is almost twice as large as the CODATA recommended value,  $R_{\text{rms}}(^1\text{H}) = 0.8414(19)$  fm. The simple reason for this discrepancy is that Eq. (B2) is a fit for atomic mass numbers  $A > 9$ , see Ref. [29]. If we use the value  $R_{\text{rms}}(^1\text{H}) = 1.406$  fm, Eq. (B1) results in  $\alpha^*(^1\text{H}) = 1.044$ , slightly larger than the value of 1.040 obtained with the CODATA  $R_{\text{rms}}(^1\text{H})$ .

The results of our calculations for  $\alpha^*$  as a function of  $Z$  are shown in Fig. 8. In this plot, the red curve represents the relationship between  $c^*/c_0$  and the nuclear charge  $Z$  of a finite-size nucleus with a Fermi charge distribution. The blue curve represents the same dependence but for a point-like nucleus, where  $\alpha^* = 1/Z$ . This parameter space can be interpreted as a phase diagram: any point  $(c/c_0, Z)$  lying above the red curve corresponds to unstable Dirac sea, where the  $1s_{1/2}$  orbital is embedded into the Dirac sea continuum.

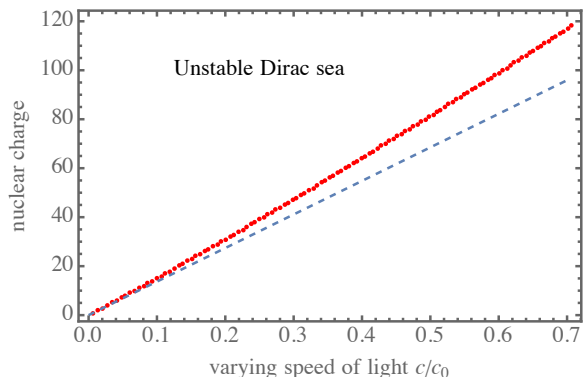


FIG. 8. Phase diagram of periodic system of elements as a function of varying speed of light. Red curve are the results for critical values of  $c^*/c_0$  as a function of nuclear charge  $Z$  for finite-size nuclei. Blue curve is the same dependence but for point-like nuclei. To borrow an analogy from condensed matter physics,  $\alpha$  (or  $c$ ) is an order parameter that governs phase transitions.

The finite-size nuclei critical curve exhibits a nearly linear dependence with a fit,

$$Z_{\text{max}} \approx 168 \frac{c}{c_0}, \quad (\text{B3})$$

or, equivalently,

$$\frac{c^*}{c_0} \approx \frac{Z}{168}. \quad (\text{B4})$$

The linearity of these equations can be understood by examining the graphical solution of the transcendental Eq. (B1), see Fig. 9 for hydrogen; plots for heavier elements are similar. Even without solving the equation (B1), it is apparent that the critical value of  $\alpha$  for the  $1s_{1/2}$  orbital occurs in the vicinity of the first zero of Macdonald function  $K_{i\nu}(\xi)$ , where the l.h.s. approaches the vertical asymptote. The first zero of  $K_{i\nu}(\xi)$  is given by  $\ln \xi \approx -\pi/\nu + \ln 2 - \gamma_{\text{Euler}}$ , where  $\gamma_{\text{Euler}} = 0.5772156649\dots$  is the Euler constant [30]. This leads to an analytical estimate

$$\alpha^* \lesssim \frac{1}{Z} \left( 1 + \frac{\pi^2}{8} \frac{1}{(\gamma_{\text{Euler}} + \frac{1}{2} \ln(\sqrt{2}ZR/a_0))^2} \right). \quad (\text{B5})$$

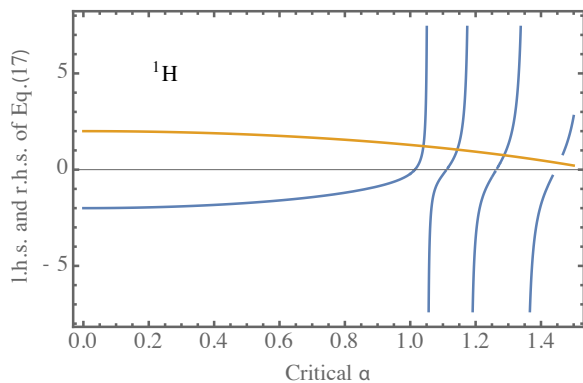


FIG. 9. Graphical determination of critical values of fine-structure constant for hydrogen ( $Z = 1, R = 0.8414$  fm). The r.h.s and the l.h.s of transcendental Eq. (B1) are drawn as blue and brown curves, respectively. The values of  $\alpha$  at the intersection of two curves are critical values  $\alpha^*$  of  $\alpha$ . The lowest  $\alpha^*$  is the critical value for  $1s_{1/2}$ , next lowest  $\alpha^*$  is for  $2s_{1/2}$  and so on.

The leading  $1/Z$  term in Eq. (B5) can be recognized as the critical value for the point-like nucleus (see the main text). We use the smaller sign ( $\lesssim$ ) because the true value of  $\alpha^*$  lies below this asymptotic estimate, see Fig. 9. The second term is due to the finite size of the nucleus, with the nuclear radius  $R \propto Z^{1/3}$ . The fractional contribution of this second term has a weak logarithmic dependence on the nuclear charge,  $\ln(Z^{4/3})$ , explaining the nearly linear dependence of the maximum allowed nuclear charge in Fig. 8. In the approximate Eq. (B5) we also restored the Bohr radius  $a_0$ , showing that the dominant dependence is the ratio of the nuclear radius  $R$  to the characteristic size of the atomic orbital  $a_0/Z$ . The approximation (B5) tends to overestimate  $\alpha^*$ . Its relative accuracy ranges from 2% for hydrogen to 50% for Fermium ( $Z = 100$ ) as follows from a comparison with our numerical results. It is worth noting also that QED

corrections to the  $1s_{1/2}$  energy (vacuum polarization and self-energy) tend to cancel [16], leaving the critical values  $\alpha^*$  and  $c^*$  largely unaffected by these corrections.

For multi-electron systems, the stability of an atom with respect to varying FCs requires further qualifiers. As discussed in the main text for hydrogen-like ions, for  $c < c^*$ , the bound  $1s_{1/2}$  level becomes embedded into the Dirac sea continuum, and, as such, becomes unstable, similar to Fano resonances in chemical physics [17]. An electron-positron pair is emitted spontaneously and the vacuum becomes electrically charged. For low-lying energy states of multi-electron atoms, however, the  $1s_{1/2}$  orbital is fully occupied. Then a Dirac sea electron can not transition into the fully occupied  $1s_{1/2}$  orbital due to the Pauli exclusion principle [15]. Yet, because the rest-mass energy gap is lowered with reduced  $c$ , ambient photons can promote Dirac sea electrons into unoccupied orbitals, i.e., Dirac sea becomes unstable with respect to the interaction with ambient photons.

As for the critical values of multi-electron systems, we computed the Dirac-Hartree-Fock (DHF) energies of the  $1s_{1/2}$  orbitals in several atoms as a function of  $c$ . We find that the hydrogen-like ion result (B3) for  $c^*$  remains an excellent approximation. Indeed, the energies of the deeply-bound  $1s_{1/2}$  orbitals in atoms and molecules are strongly dominated by the interaction with the nucleus with a small corrections from the interaction with other electrons.

### Appendix C: Results for many-electron atoms

The atomic spectra of N, O, F, and Ne atoms were calculated at different values of the speed of light (or  $\alpha$ ) using the Kramer Restricted Configuration Interaction (KR CI) method, as implemented in DIRAC19 [12, 13]. The Dirac-Hartree-Fock (DHF) calculations were first carried out to obtain the reference wavefunction for the CI step. In the DHF calculations, the  $3s_{1/2}$  orbital was included in the active space via the average-of-configuration open-shell framework [12]. This ensures the balanced description of atomic states at the CI step and allows us to assess the effects of the relativistic stabilization of the  $3s_{1/2}$  orbital.

At the nominal  $c$ , the atomic states are labeled in the conventional L-S (Russell-Saunders) coupling scheme:  $2S+1L_J$ . At decreased  $c$ , however, the amplified relativity leads to the breakdown of the LS coupling scheme, as only the total angular momentum  $J$ ,  $\mathbf{J} = \mathbf{L} + \mathbf{S}$ , is conserved [28]. Thereby, we label the states as  $J^\pi$ , where  $J$  is the value of the total angular momentum and  $\pi$  is the parity of the state. If there are multiple states of the same  $J^\pi$  symmetry, we distinguish them by appending their sequential number  $n$ :  $J^\pi(n)$ , where the states are enumerated in the order of increasing energy. In our notation for electronic configurations, for brevity, we suppress the  $1s_{1/2}$  and  $2s_{1/2}$  shells, as these remain always doubly occupied for our considered low-lying en-

ergy states.

Since the typical distance of an electron from the nucleus decreases with  $c$  due to relativistic contraction, the basis sets used in our calculations needed to be calibrated to accurately describe the electronic density near the nucleus at reduced  $c$ . The calibrating procedure was carried out by considering the hydrogen-like ions of N, O, F, and Ne as follows. For a selected ion, the speed of light was gradually lowered until the  $1s_{1/2}$  ground state dived into the Dirac sea. The size of the basis set and the largest exponents were chosen to match the critical values of  $c^*$  obtained using such a basis set with that predicted by solving the transcendental Eq. (B1). Additionally, the validity of these basis sets was verified by comparing the energy level orderings they generated with those predicted by the finite-difference solution of the Dirac equation. To obtain the correct energy ordering, it required to augment standard basis sets with additional  $p$  basis functions.

For example, for N, the eleven  $p$  basis functions in the original unc-aug-cc-pV6Z basis set were augmented to a total of nineteen. The exponents of the new functions were obtained by subsequently multiplying the largest  $p$  exponent by 3. For simplicity, the same exponents were used for the  $s$  basis functions. This procedure was carried out until a match with the solution to the transcendental Eq. (B1) was obtained, while maintaining the correct ordering of the energy levels. The resulting modified basis thus included nineteen  $s$  and nineteen  $p$  basis functions with the largest exponent being  $6.9 \times 10^8$ . Basis functions of higher angular momenta were left unchanged. The same strategy was used for O, F, and Ne, yielding modified basis sets containing also nineteen  $s$  and nineteen  $p$  basis functions. The largest exponents were, respectively,  $8.8 \times 10^8$  for O,  $1.1 \times 10^9$  for F, and  $1.4 \times 10^9$  for Ne. With such modified basis sets, the critical  $c^*$  values obtained using the DIRAC19 program matched those predicted by Eq. (B1), namely, the critical values are  $c_N^* \approx c_0/21.1$ ,  $c_O^* \approx c_0/18.4$ ,  $c_F^* \approx c_0/16.4$ , and  $c_{Ne}^* \approx c_0/14.8$ .

Note that to avoid the collapse of many-electron wavefunctions into the Dirac sea [31], the so-called ‘‘no-pair’’ Hamiltonian [32, 33] was used in fully relativistic electronic structure calculations

$$H_{\text{no-pair}} = \sum_i h_D(i) + \frac{1}{2} \sum_{i \neq j} \Lambda_{++} \frac{1}{r_{ij}} \Lambda_{++}. \quad (\text{C1})$$

Here the first term is a sum of the Dirac Hamiltonian  $h_D(i)$  describing an electron  $i$  moving in the potential of a finite-size nucleus and the second term describes the Coulomb repulsion between the electrons. Notice that the  $e - e$  interaction is sandwiched between projection operators  $\Lambda_{++}$  which exclude states from the Dirac sea continuum of  $h_D$ .

We have described the methods with which we computed the low-lying energy states of several second-period atoms, from nitrogen through to neon, at the nominal

and reduced speeds of light. Below, we present the results of our calculations. We find that as  $c$  is reduced, the energies of the excited states of an atom exhibit various interesting features. Relative to the energy of the ‘‘nominal’’ ground state (the ground state at nominal  $c$ ), an excited state energy may rise or fall in the regime  $c \sim c_0/10$ , leading to several crossings of levels. However, as  $c$  is reduced further, all excited states eventually stabilize with respect to the nominal ground state. Even more remarkably, as  $c$  nears  $c^*$ , the energies of some excited states decrease so much that these states become the ‘‘new’’ ground states themselves. This phenomenon happens in all considered atoms, albeit to different degrees: in F, the change in the nature of the ground state only lasts for a small interval of  $c$  around  $c_0/15$ , whereas in N, O, and Ne, the ‘‘usurping’’ excited states remain the ground state of their respective atoms until  $c$  reaches  $c^*$ .

We show below that the electron-configuration picture is sufficient for the qualitative explanation of these phenomena. The lynch-pins of this exposition are the facts that as  $c$  decreases, (i) the  $2p_{1/2}$  energy decreases, (ii) the  $2p_{3/2}$  energy increases, (iii) the  $3p_{1/2}$  energy falls, but with a slower rate than that of  $2p_{1/2}$ , (iv) the  $3p_{3/2}$  energy rises but with a slower rate than that of  $2p_{3/2}$ , and (v) all  $s_{1/2}$  energies fall. It is worth stressing that the rise in the energy of  $2p_{3/2}$  (and similarly of all other  $p_{3/2}$ ) orbitals is only present in multi-electron atoms. In a hydrogen-like atom, although the fine-structure contribution to a  $2p_{3/2}$  energy increases with decreasing  $c$ , the gross-structure contribution decreases (it is a negative quantity whose magnitude gets larger), leading to an overall decline of the  $2p_{3/2}$  energy. In a multi-electron atom, however, the contractions of the inner  $1s_{1/2}$ ,  $2s_{1/2}$ , and  $2p_{1/2}$  orbitals with decreasing  $c$  leads to more effective screening of the nuclear charge, thus reducing the magnitude of the gross-structure contribution to the  $2p_{3/2}$  energy. This in turn means that the  $2p_{3/2}$  energy increases with decreasing  $c$ .

### 1. Nitrogen ( $c^* \approx c_0/21.1$ )

We begin our discussion with the nitrogen atom, describing the changes in its eight lowest energy states induced by varying  $c$ , see Fig. 10. The  $2p^3$  ground electron configuration of the nitrogen atom produces five states which arises from all possible distributions of the three valence electrons over the six orbitals  $2p_{1/2,\pm 1/2}$ ,  $2p_{3/2,\pm 1/2}$ , and  $2p_{3/2,\pm 3/2}$ . The ground state, labeled as  $^4S_{3/2}^o$  at  $c = c_0$ , is the spin quartet with the total orbital angular momentum  $L = 0$ . The left superscript is the spin multiplicity  $2S + 1$ , and the right superscript  $o$  indicates an odd parity.

The excited states of the  $2p^3$  configuration at the nominal  $c$  are the spin doublet states  $^2D^o$  and  $^2P^o$ , with orbital angular momenta  $L = 2$  and  $L = 1$ , respectively. The  $^2D^o$  and  $^2P^o$  states both split into components with different values of the total angular momentum quan-

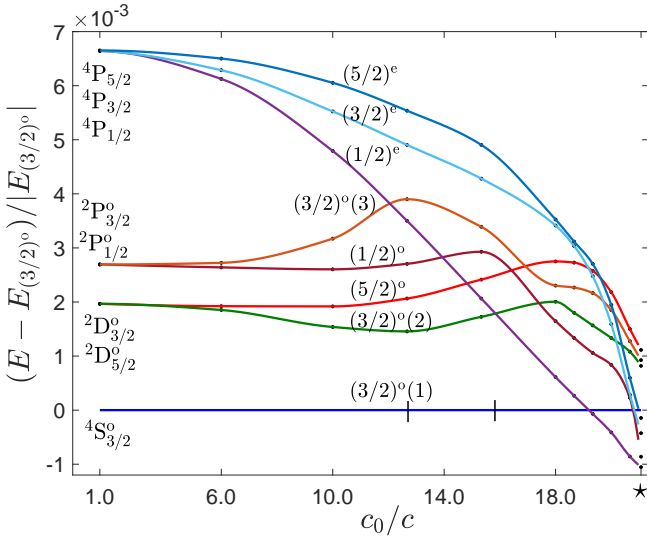


FIG. 10. Energy spectrum of nitrogen atom as a function of speed of light (or  $\alpha$ ). The critical value of the speed of light is marked with star ( $\star$ ).

tum number  $J$ . Namely, the  ${}^2D^o$  state splits into the  ${}^2D_{5/2}^o$  and  ${}^2D_{3/2}^o$  states, whereas the  ${}^2P^o$  state — into the  ${}^2P_{1/2}^o$  and  ${}^2P_{3/2}^o$  states. The first excited configuration  $2p^23s$  produces the following quartet states of even parity:  ${}^4P_{1/2}$ ,  ${}^4P_{3/2}$ , and  ${}^4P_{5/2}$ .

At  $c < c_0$ , the eight states are labeled as  $(3/2)^o(1)$ ,  $(5/2)^o$ ,  $(3/2)^o(2)$ ,  $(1/2)^o$ ,  $(3/2)^o(3)$ ,  $(1/2)^e$ ,  $(3/2)^e$ , and  $(5/2)^e$ , respectively, using the  $J^\pi$  notation. Throughout this discussion, the nominal ground state  $(3/2)^o(1)$ , which corresponds to  ${}^4S_{3/2}$  at  $c = c_0$ , is used as a reference; and all state energies are reported as the ratio  $(E - E_{(3/2)^o})/|E_{(3/2)^o}|$ .

This choice does not imply, however, that the energy of  $(3/2)^o(1)$  remains unaffected as  $c$  decreases. In fact, the dominant electron configuration of  $(3/2)^o(1)$  changes twice within the range  $c^* \leq c < c_0$ . In the range  $c_0/13 \lesssim c < c_0$ , the dominant configurations are  $2p_{1/2}^2 2p_{3/2}$ ,  $2p_{1/2} 2p_{3/2}^2$ , and  $2p_{3/2}^3$ . As  $c$  decreases, the energy of the  $2p_{1/2}$  orbital decreases while that of  $2p_{3/2}$  increases [34] until, at  $c \lesssim c_0/13$ , the  $2p_{3/2}^3$  configuration becomes energetically unfavorable and no longer contributes to the ground state. Furthermore, since the  $3p_{3/2}$  orbital is further away from the nucleus than the  $2p_{3/2}$  orbital, the former is less influenced by relativistic effects than the latter (recall that, at least in the regime of small  $\alpha$ , the spin-orbit splitting scales as  $n^{-3}$  where  $n$  is the principle quantum number). As a result, the  $2p_{1/2} 2p_{3/2}^2$  configuration eventually becomes less energetically favorable than, and is thus replaced by  $2p_{1/2}^2 3p_{3/2}$ . This happens at  $c \approx c_0/15$ . We now discuss the behavior of the four components of the  ${}^2D^o$  and  ${}^2P^o$  doublets with respect to changing  $c$ .

For  $c_0/13 \lesssim c < c_0$ , the state  $(3/2)^o(2)$  has domi-

nant configurations  $2p_{1/2} 2p_{3/2}^2$  and  $2p_{1/2}^2 2p_{3/2}$  whereas the ground state contains the extra  $2p_{3/2}^3$ . Since the  $2p_{3/2}$  energy increases with decreasing  $c$ , this leads to a slight stabilization of  $(3/2)^o(2)$  with respect to the ground state. For  $c_0/18 \lesssim c < c_0/13$ , however, the configuration  $2p_{3/2}^3$  drops off from the ground state and  $2p_{1/2}^2 2p_{3/2}$  drops off from  $(3/2)^o(2)$ , leading to the destabilization of  $(3/2)^o(2)$ . At  $c \approx c_0/18$ , however, an avoided crossing happens between  $(3/2)^o(2)$  and  $(3/2)^o(3)$ , at which point the dominant configuration of  $(3/2)^o(2)$  becomes  $2p_{1/2}^2 3p_{3/2}$  and remains so thereafter. This is to be compared with the ground state, whose composition involves  $2p_{1/2}^2 3p_{3/2}$  and  $2p_{1/2}^2 2p_{3/2}$ . Since the  $3p_{3/2}$  energy increases at a much slower rate than that of  $2p_{3/2}$ , this results in the eventual stabilization of  $(3/2)^o(2)$  with respect to the ground state.

Next, we discuss the state  $(5/2)^o$ , whose dominant configuration  $2p_{1/2} 2p_{3/2}^2$  remains the same throughout the variation of  $c$ . In the regime  $c_0/13 \lesssim c \leq c_0$ , the  $(5/2)^o$  energy remains stable relative to that of the ground state  $(3/2)^o(1)$  due to the balance between the  $2p_{1/2}^2 2p_{3/2}$  and  $2p_{3/2}^3$  configurations in the latter. However, as soon as  $2p_{3/2}^3$  drops off from  $(3/2)^o(1)$  at  $c \approx c_0/13$ , the state  $(5/2)^o$  starts to destabilize relative to the ground state. This trend continues past  $c \approx c_0/15$ , where the ground state composition changes to  $2p_{1/2}^2 2p_{3/2}$  and  $2p_{1/2}^2 3p_{3/2}$ , until  $c \approx c_0/18$ , at which point correlation effects, especially interactions with higher-lying states of the same  $J$  and parity, force the  $(5/2)^o$  energy down. This results in the stabilization of  $(5/2)^o$  relative to the ground state for  $c \lesssim c_0/18$ .

Before describing the behavior of the remaining two states of the  ${}^2D^o$  and  ${}^2P^o$  doublets, we note that the  $(5/2)^o$  and  $(3/2)^o(2)$  states cross at  $c \approx c_0/3$ . At the nominal  $c$ ,  $(5/2)^o$  is around  $8 \text{ cm}^{-1}$  lower in energy than  $(3/2)^o(2)$ . In the region  $c_0/7 \leq c < c_0$ , both states are dominated by the  $2p_{1/2} 2p_{3/2}^2$  configuration. However, the  $(3/2)^o(2)$  state, due to its lower value of  $J$ , contains a second dominant configuration,  $2p_{1/2}^2 2p_{3/2}$ . As  $c$  decreases, this extra configuration is responsible for the stabilization of  $(3/2)^o(2)$  relative to  $(5/2)^o$ .

We now turn our attention to the state  $(1/2)^o$ . In the regime  $c_0/15 \lesssim c \leq c_0$ , its dominant configuration is  $2p_{1/2} 2p_{3/2}^2$ , the same as for  $(5/2)^o$ . As a result, the  $(1/2)^o$  energy behaves in a similar way as that of  $(5/2)^o$ : relative to the ground state energy, it remains stable for  $c_0/13 \lesssim c \leq c_0$  and rises for  $c_0/15 \lesssim c \leq c_0/13$ . At  $c \approx c_0/15$ , however, the avoided crossing with a higher (nominally)  $S_{1/2}^o$  state causes the configuration of  $(1/2)^o$  to become  $2p_{1/2}^2 3p_{1/2}$ , which results in  $(1/2)^o$  rapidly stabilizing with respect to the ground state.

Finally, we discuss the state  $(3/2)^o(3)$ . For  $c_0/6 \lesssim c \leq c_0$ , the dominant configuration in  $(3/2)^o(3)$  is  $2p_{1/2}^2 2p_{3/2}$  with a small mixture of  $2p_{3/2}^3$ . As a result, in this regime, the energy of  $(3/2)^o(3)$  remains stable relative to that of

the ground state  $(3/2)^o(1)$ . As  $c$  decreases further, the contributions from  $2p_{3/2}^3$  to  $(3/2)^o(3)$  grows and eventually becomes dominant, leading to a rapid destabilization of  $(3/2)^o(3)$  with respect to  $(3/2)^o(1)$ . One would expect this destabilization to accelerate when  $c$  decreases past the value  $c_0/13$ , whereupon  $2p_{3/2}^3$  drops off from the ground state configuration. However, at  $c \approx c_0/13$ , the avoided crossing between  $(3/2)^o(3)$  and the higher-lying  $(3/2)^o(4)$  changes the dominant configuration of  $(3/2)^o(3)$  to  $2p_{1/2}^2 3p_{3/2}$ . This leads to a rapid downturn of the  $(3/2)^o(3)$  energy relative to that of  $(3/2)^o(1)$ . As noted above, at  $c \approx c_0/18$ , another avoided crossing, this time between  $(3/2)^o(3)$  and  $(3/2)^o(2)$ , occurs, changing the nature of  $(3/2)^o(3)$  to  $2p_{1/2} 2p_{3/2}^2$ . As  $c$  decreases, the “new” state  $(3/2)^o(3)$  stabilizes further due to correlation effects.

We have described the behaviors of the four lowest excited odd-parity states as  $c$  varies. We now extend our discussion to the three lowest even-parity states  $(1/2)^e$ ,  $(3/2)^e$  and  $(5/2)^e$  states, which at the nominal  $c$  correspond to  $^4P_{1/2}$ ,  $^4P_{3/2}$  and  $^4P_{5/2}$ . For this purpose, apart from the observation that the  $2p_{1/2}$  energy decreases while the  $2p_{3/2}$  energy increases as  $c$  is reduced, we also need the fact that the  $3s_{1/2}$  energy decreases with decreasing  $c$  [34].

We begin with the state  $(1/2)^e$ . Near the nominal  $c$ , it comprises of the  $2p_{1/2}^2 3s_{1/2}$ ,  $2p_{3/2}^2 3s_{1/2}$ , and  $2p_{1/2} 2p_{3/2} 3s_{1/2}$  configurations. As  $c$  decreases, the destabilizing  $2p_{3/2}$  orbital causes the last two configurations to drop off, at  $c \approx c_0/10$ . The remaining configuration  $2p_{1/2}^2 3s_{1/2}$ , which contains only stabilizing orbitals, causes the  $(1/2)^e$  energy to decline rapidly, until  $c \approx c_0/19$ , where it falls below the energy of  $(3/2)^o(1)$  and  $(1/2)^e$  becomes the new ground state of nitrogen.

Similarly, at  $c = c_0$ ,  $(3/2)^e$  and  $(5/2)^e$  are mixtures of the  $2p_{3/2}^2 3s_{1/2}$  and  $2p_{1/2} 2p_{3/2} 3s_{1/2}$  configurations, with  $2p_{3/2}^2 3s_{1/2}$  dropping off at  $c \lesssim c_0/15$ . That these two states have the same dominant configuration for  $c \lesssim c_0/15$  is evident via the near coincidence of the two corresponding curves in this regime, see Fig. 10. That their dominant configuration for small  $c$  still containing the destabilizing orbital  $2p_{3/2}$  also explains why the  $(3/2)^e$  and  $(5/2)^e$  energies do not decline as fast as that of  $(1/2)^e$ . As a result, although their energies do fall below that of the nominal ground state  $(3/2)^o(1)$ ,  $(3/2)^e$  and  $(5/2)^e$  lose out in the competition with  $(1/2)^e$  to become the new ground state of nitrogen.

## 2. Oxygen ( $c^* \approx c_0/18.4$ )

In this subsection, we turn to the discussion of the oxygen atom, where we consider five lowest states of even parity, nominally  $^3P_2$ ,  $^3P_1$ ,  $^3P_0$ ,  $^1D_2$ , and  $^1S_0$ , originating from the  $2p^4$  ground electron configuration of oxygen, and the two lowest odd-parity excited states  $^5S_2^o$  and  $^3S_1^o$ , originating from the  $2p^3 3s$  configuration, see Fig. 11. The

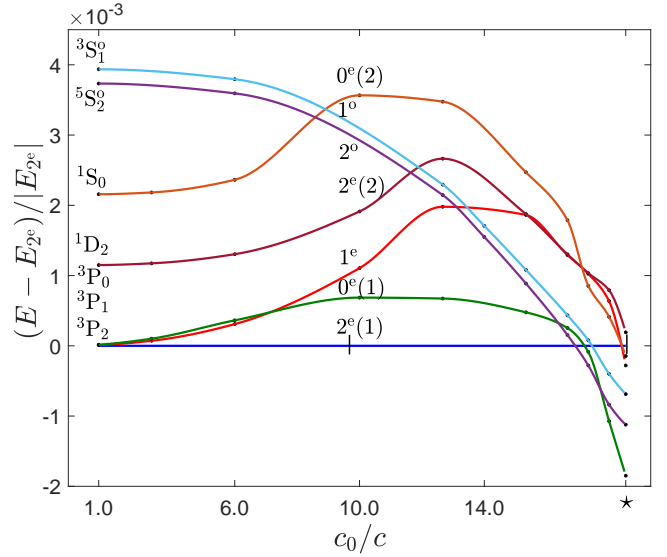


FIG. 11. Energy spectrum of oxygen atom as a function of speed of light (or  $\alpha$ ). The critical value of  $c_0/c$  is marked with star ( $\star$ ).

nominal ground state of oxygen, labeled as  $^3P_2$  at  $c = c_0$  and  $2^e(1)$  for  $c < c_0$ , is used as a reference.

Just like for nitrogen, we begin by describing the behavior of the nominal ground state with decreasing  $c$ . In the regime  $c_0/10 \lesssim c \leq c_0$ ,  $2^e(1)$  comprises predominantly of  $2p_{1/2}^2 2p_{3/2}^2$  and  $2p_{1/2} 2p_{3/2}^3$ . For  $c \lesssim c_0/10$ , the  $2p_{3/2}$  energy rises high enough so that the contribution of  $2p_{1/2} 2p_{3/2}^3$  becomes subdominant. At  $c \approx c^* \approx c_0/18.4$ , the energies of the stabilizing orbital  $3s_{1/2}$  and that of the destabilizing orbital  $2p_{3/2}$  become nearly degenerate. As a result, two  $p$ -shell electrons may be promoted to the  $3s_{1/2}$  shell and  $2p_{1/2} 2p_{3/2} 3s_{1/2}^2$  emerges as a dominant configuration in  $2^e(1)$ . Note that this promotion involves one  $2p_{1/2}$  and one  $2p_{3/2}$  electron due to the conservation of total angular momentum and parity.

Next, we concentrated on the excited states. For  $c_0/10 \lesssim c \leq c_0$ , the state  $0^e(1)$ , which at  $c = c_0$  is labeled  $^3P_0$ , is a mixture of  $2p_{1/2}^2 2p_{3/2}^2$  and  $2p_{3/2}^4$ . Since  $0^e(1)$  contains a configuration which has the destabilizing orbital  $2p_{3/2}$  quadruply occupied, in contrast to  $2^e(1)$ , in whose configurations  $2p_{3/2}$  is at most triply occupied,  $0^e(1)$  destabilizes relative to the ground state in this regime. For  $c < c_0/10$ , the contribution  $2p_{3/2}^4$  is no longer significant, leaving only  $2p_{1/2}^2 2p_{3/2}^2$  as the dominant configuration in the CI expansion of  $0^e(1)$ , similar to  $2^e(1)$ . This explains the flattening out of the  $0^e(1)$  curve in the regime  $c_0/13 \lesssim c \lesssim c_0/10$ . For  $c \lesssim c_0/13$ , however, the state  $0^e(1)$  begins to stabilize relative to the ground state. This is due to the avoided crossing with  $0^e(2)$ , which introduces the configuration  $2p_{1/2}^2 3s_{1/2}^2$  to the CI expansion of  $0^e(1)$ . The doubly-occupied stabilizing  $3s_{1/2}$  orbital causes the  $0^e(1)$  energy to decline rapidly and eventually fall below that of  $2^e(1)$  at  $c \approx c_0/17$ ,

making  $0^e(1)$  the new ground state of oxygen.

We now address the state  $1^e$ , which at  $c = c_0$  is labeled  $3P_1$ . For  $c_0/13 \lesssim c \leq c_0$ , the dominant configuration of  $1^e$  is  $2p_{1/2}2p_{3/2}^3$ , which means that this state destabilizes relative to the nominal ground state (the rate of destabilization increases after  $c \approx c_0/10$ , when  $2p_{1/2}2p_{3/2}^3$  is no longer a dominant contribution to the ground state). However, at  $c \approx c_0/13$ , the energy of  $3p_{1/2}$  is lowered enough so that the configuration  $2p_{1/2}^22p_{3/2}3p_{1/2}$  emerges in the expansion of  $1^e$ . Notice that the transfer of one  $2p_{3/2}$  electron to the  $3p_{1/2}$  shell is accompanied by the demotion of another  $2p_{3/2}$  electron to the  $2p_{1/2}$  shell in order to conserve total angular momentum. The stabilizing orbital  $3p_{1/2}$  causes the  $1^e$  energy to decrease relative to and eventually become lower than that of the nominal ground state. However, the stabilization effect of the singly-occupied  $3p_{1/2}$  orbital is not as strong as that of the doubly-occupied  $3s_{1/2}$  orbital so  $1^e$  never becomes the new ground state in place of  $0^e(1)$ .

Before discussing the remaining states, we note that similar to nitrogen, there occurs an “early” crossing between the  $1^e$  and  $0^e(1)$  states of the oxygen atom, see Fig. 11. At  $c = c_0$ ,  $0^e(1)$  lies  $65 \text{ cm}^{-1}$  higher in energy than  $1^e$ . At  $c \approx c_0/7$ , the role of  $2p_{3/2}^4$  in  $0^e(1)$  starts to diminish and since the remaining configuration  $2p_{1/2}^22p_{3/2}^2$  of  $0^e(1)$  is more energetically favorable than the  $2p_{1/2}2p_{3/2}^3$  of  $1^e$ ,  $0^e(1)$  crosses below  $1^e$ .

We continue our discussion with the state  $2^e(2)$  which is labeled  $1D_2$  at  $c = c_0$ . In the regime  $c_0/10 \lesssim c \leq c_0$ ,  $2^e(2)$  is made up of  $2p_{1/2}^22p_{1/2}^2$  and  $2p_{1/2}2p_{1/2}^3$ , similar to the ground state  $2^e(1)$ , albeit with different proportions of the configurations. As  $c$  decreases, the  $2p_{1/2}2p_{1/2}^3$  component becomes more and more pronounced in  $2^e(2)$  instead of fading out as in  $2^e(1)$ . At  $c \approx c_0/10$ ,  $2p_{1/2}2p_{1/2}^3$  drops off from the ground state configuration whereas it becomes the dominant contribution to  $2^e(2)$ . These two observations are supported by the upturn of the  $2^e(2)$  curve relative to the ground state baseline. At  $c \approx c_0/13$ , however,  $2^e(2)$  participates in an avoided crossing with the  $2^e(3)$  (nominally  $5P_2$ ) state, whereupon its configuration becomes a mixture of  $2p_{1/2}^22p_{3/2}3p_{1/2}$  and  $2p_{1/2}2p_{3/2}^23p_{1/2}$ . The presence of the  $3p_{1/2}$  orbital causes  $2^e(2)$  to stabilize relative to the ground state, albeit not strongly enough to drive it below  $2^e(1)$  before  $c$  reaches  $c^*$ .

The last even-parity state in our current discussion of the oxygen atom is  $0^e(2)$ , which is labeled  $1S_0$  at  $c = c_0$ . For  $c_0/10 \lesssim c \leq c_0$ , the state  $0^e(2)$  comprises of the configurations  $2p_{1/2}^22p_{3/2}^2$  and  $2p_{3/2}^4$ , with the latter causing the  $0^e(2)$  energy to rise relative to that of the ground state. At  $c \approx c_0/10$ , however, there occurs an avoided crossing between  $0^e(2)$  and the higher lying  $0^e(3)$  state (not shown), whereupon the dominant configuration in  $0^e(2)$  changes to  $2p_{1/2}^22p_{3/2}3p_{3/2}$ . As  $c$  decreases further, this configuration becomes more and more dominant in  $0^e(2)$ , thus stabilizing this state relative to the ground

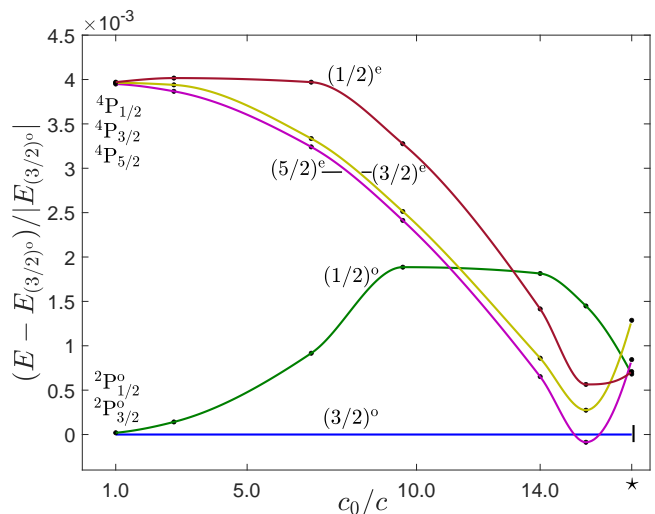


FIG. 12. Energy spectrum of fluorine atom as a function of speed of light (or  $\alpha$ ). The critical value of  $c_0/c$  is marked with star ( $\star$ ).

state, which, to reiterate, comprises mainly of  $2p_{1/2}^22p_{3/2}^2$ . At even smaller  $c$ , more specifically, at  $c \approx c_0/12$ ,  $0^e(2)$  becomes involved in another avoided crossing with the same  $0^e(3)$ . After this second avoided crossing, the dominant configuration in  $0^e(2)$  is now  $2p_{1/2}^23s_{1/2}^2$ , which causes its energy to fall even more precipitously. The state  $0^e(2)$  does eventually fall below the nominal ground state but this happens very close to the critical  $c^*$ .

Finally, we discuss the two odd-parity states,  $2^o$  and  $1^o$ , which, at  $c = c_0$ , are labeled  $5S_2^o$  and  $3S_1^o$ , respectively. The evolutionary patterns of these two states as  $c$  varies are qualitatively the same, as evident in the congruence of their corresponding curves. They start out as combinations of  $2p_{1/2}^22p_{3/2}3s_{1/2}$ ,  $2p_{1/2}2p_{3/2}^23s_{1/2}$ , and  $2p_{3/2}^33s_{1/2}$ . For  $c_0/6 \lesssim c \leq c_0$ , the competing lowering of the  $3s_{1/2}$  energy and raising of the  $2p_{3/2}$  energy results in a slight stabilization of  $2^o$  and  $1^o$  relative to the ground state. However, for  $c \lesssim c_0/6$ , the two configurations with  $2p_{3/2}$  doubly and triply occupied drop off from the CI expansions of  $2^o$  and  $1^o$ , leaving only  $2p_{1/2}^22p_{3/2}3s_{1/2}$  which hastens their stabilization. In fact, the state  $2^o$  is the first to come below the nominal ground state  $2^e(1)$ , at  $c \approx c_0/16.5$ , thus acting as a “new” ground state in the interval  $c_0/17 \lesssim c \lesssim c_0/16.5$ , after which the role of ground state is taken over by  $0^e(1)$ . Although the state  $1^o$  does cross the nominal ground state, at  $c \approx c_0/17$ , its higher energy at  $c = c_0$  means that it never becomes a ground state of oxygen, unlike  $2^o$ .

### 3. Fluorine ( $c^* \approx c_0/16.4$ )

In this subsection, we investigate the behavior of atomic fluorine with varying  $c$ , limiting ourselves to the five lowest states, see Fig. 12. At the nominal  $c$ , the  $2p^5$

ground electron configuration produces two atomic states with odd parities,  ${}^2P_{3/2}^o$  and  ${}^2P_{1/2}^o$ . From the  $2p^43s$  first excited configuration of fluorine we consider three lowest-lying states, which are labeled  ${}^4P_{5/2}$ ,  ${}^4P_{3/2}$ , and  ${}^4P_{1/2}$  at  $c = c_0$ .

Again, the nominal ground state, labeled  $(3/2)^o$  for  $c < c_0$ , is used as a reference. It consists of a single dominant configuration  $2p_{1/2}^22p_{3/2}^3$  from  $c = c_0$  all the way down to  $c \approx c_0/14$  where next possible configuration,  $2p_{1/2}^22p_{3/2}3s_{1/2}^2$  as required by the conservation of total angular momentum and parity, emerges as another dominant configuration. This fact may be understood by noting that  $2p_{1/2}^22p_{3/2}3s_{1/2}^2$  involves transferring a pair of  $2p_{3/2}$  electrons to the higher  $3s_{1/2}$  shell and is thus only possible if the  $3s_{1/2}$  and  $2p_{3/2}$  energies are close enough to each other.

We now discuss the odd-parity excited states. In the region  $c_0/10 \lesssim c < c_0$ , the state  $(1/2)^o$  (nominally  ${}^2P_{1/2}^o$ ) consists primarily of  $2p_{1/2}2p_{3/2}^4$ , so its energy rises relative to that of the ground state  $(3/2)^o$ . At  $c \lesssim c_0/10$ , however, the  $2p_{3/2}$  and  $3p_{3/2}$  energies come close enough to one another so that the migration of a  $2p_{3/2}$  electron to the  $3p_{3/2}$  shell happens, accompanied by the filling of the  $2p_{1/2}$  shell with another  $2p_{3/2}$  electron. As a result,  $(1/2)^o$  acquires the component  $2p_{1/2}^22p_{3/2}^23p_{3/2}$ , which causes its energy to slightly lower relative to the ground state energy. When  $c$  is reduced beyond  $c_0/14$ , the energy gaps between  $2p_{3/2}$  and  $3s_{1/2}$  and between  $3p_{1/2}$  and  $3p_{3/2}$  become such that it is possible to promote the two  $2p_{3/2}$  electrons to  $3s_{1/2}$  while demoting at the same time the  $3p_{3/2}$  electron to  $3p_{1/2}$ . As a result, for  $c \lesssim c_0/14$ , the state  $(1/2)^o$  contains the configuration  $2p_{1/2}^23s_{1/2}^23p_{1/2}$ . The stabilizing  $3s_{1/2}$  and  $3p_{1/2}$  orbitals cause a rapid decline in the  $(1/2)^o$  as  $c$  approaches  $c^*$ .

We now describe the even-parity states. The behaviors of  $(5/2)^e$  and  $(3/2)^e$  (nominally  ${}^4P_{5/2}$  and  ${}^4P_{3/2}$ , respectively) as  $c$  varies are very similar. They both start out as combinations of  $2p_{1/2}^22p_{3/2}^23s_{1/2}$  and  $2p_{1/2}2p_{3/2}^33s_{1/2}$ . The configuration  $2p_{1/2}^22p_{3/2}^23s_{1/2}$  is responsible for the stabilization of these two states relative to  $(3/2)^o$ . This stabilization is gradual at first but accelerates after  $c \approx c_0/2$ , when the energetically unfavorable component  $2p_{1/2}2p_{3/2}^33s_{1/2}$  drops off from the CI expansion of  $(5/2)^e$  and  $(3/2)^e$ . As  $c$  is reduced further to  $c \approx c_0/14$ , the configuration  $2p_{1/2}^22p_{3/2}3s_{1/2}^2$  appears in the expansion of the ground state and, since the  $3s_{1/2}$  energy is still a little higher than that of  $2p_{3/2}$ , causes the states  $(5/2)^e$  and  $(3/2)^e$  to stabilize even faster. In fact,  $(5/2)^e$  briefly replaces  $(3/2)^o$  as the “new” ground state of fluorine. At  $c \approx c_0/15$ , however, the  $3s_{1/2}$  energy falls below that of  $2p_{3/2}$  and this explains the upturn at the rightmost ends of the  $(5/2)^e$  and  $(3/2)^e$  energy curves.

Finally, we discuss the state  $(1/2)^e$  which is labeled  ${}^4P_{1/2}$  at  $c = c_0$ . For  $c_0/6 \lesssim c < c_0$ , its CI expansion contains the configurations  $2p_{1/2}^22p_{3/2}^23s_{1/2}$ ,  $2p_{1/2}2p_{3/2}^33s_{1/2}$ , and  $2p_{3/2}^43s_{1/2}$ . The stabilization of  $2p_{1/2}$  and  $3s_{1/2}$  com-

petes with the destabilization of  $2p_{3/2}$ , resulting in a flat pattern of the  $(1/2)^e$  energy relative to the ground state energy. For  $c$  below  $c_0/6$ , however, the two configurations with  $2p_{3/2}$  triply and quadruply occupied become so energetically unfavorable that they no longer contribute to  $(1/2)^e$ . The remaining configuration  $2p_{1/2}^22p_{3/2}^23s_{1/2}$  leads to a rapid downturn of the  $(1/2)^e$  energy. The rise of the  $(1/2)^e$  energy relative to the ground state for  $c \lesssim c_0/16$  may again be explained by the crossing of the  $2p_{3/2}$  and  $3s_{1/2}$  orbitals.

#### 4. Neon ( $c^* \approx c_0/14.8$ )

The last atom in our consideration is neon. At the nominal  $c = c_0$ , the closed-shell  $2p^6$  ground electron configuration  $2p^6$  of neon results in a single atomic state with even parity,  ${}^1S_0$ . The  $2p^53s$  first excited configuration gives rise to four excited states with odd parity:  ${}^2[3/2]_2^o$ ,  ${}^2[3/2]_1^o$ ,  ${}^2[1/2]_0^o$ , and  ${}^2[1/2]_1^o$ . The second excited configuration,  $2p^53p$ , generates a manifold of atomic states with even parity, among which we consider the three lowest states,  ${}^2[1/2]_1$ ,  ${}^2[5/2]_3$ , and  ${}^2[5/2]_2$ . We therefore include a total of eight atomic states of neon in our discussion, see Fig. 3 in the main text. At smaller  $c$ , these states are labeled, in the order they are introduced above, as  $0^e$ ,  $2^o$ ,  $1^o(1)$ ,  $0^o$ ,  $1^o(2)$ ,  $1^e$ ,  $3^e$ , and  $2^e$ , respectively.

Again, we use the nominal ground state  $0^e$ , corresponding to  ${}^1S_0$  at the nominal  $c$ , as a reference. In the range  $c_0/13 \lesssim c \leq c_0$ , the  $0^e$  state retains  $0^e$  its closed-shell configuration of  $2p_{1/2}^22p_{3/2}^4$ . At  $c \approx c_0/13$ , the  $3s_{1/2}$  and  $2p_{3/2}$  energies become close enough so that  $2p_{1/2}^22p_{3/2}^23s_{1/2}$  emerges as an appreciable contribution in the CI expansion of  $0^e$ . Note that two electrons are transferred from  $2p_{3/2}$  to  $3s_{1/2}$  to preserve total angular momentum and parity. The appearance of the open-shell configuration  $2p_{1/2}^22p_{3/2}^23s_{1/2}$  in the CI expansion of the nominal ground state indicates that at  $c \lesssim c_0/14$ , neon is no longer chemically inert.

The fact that lowering  $c$  has the effect of “activating” the naturally inert neon may also be understood by considering the state  $2^o$ , which corresponds to  ${}^2[3/2]_2^o$  at  $c = c_0$ . The main configuration for  $2^o$  in the regime  $c_0/13 \lesssim c \leq c_0$  is  $2p_{1/2}^22p_{3/2}^33s_{1/2}$  containing the orbital  $3s_{1/2}$  which has the effect of destabilizing  $2^o$ . As discussed in the previous paragraph, in the vicinity of  $c \approx c_0/13$ , the ground state  $0^e$  acquires the component  $2p_{1/2}^22p_{3/2}^23s_{1/2}$ . Since the  $3s_{1/2}$  orbital still lies above  $2p_{3/2}$  in this regime, the  $2^o$  energy falls below that of  $0^e$  and  $2^o$  briefly becomes the “new” ground state of neon. However, as  $c$  nears  $c_0/14$ , the  $2p_{3/2}$  and  $3s_{1/2}$  orbitals cross, raising  $2^o$  back above  $0^e$ .

The state  $1^o(1)$  (nominally  ${}^2[3/2]_1^o$ ) displays a dependence on varying  $c$  similar to that of  $2^o$ . In the regime  $c_0/13 \lesssim c \leq c_0$ , its CI expansion is dominated by  $2p_{1/2}^22p_{3/2}^33s_{1/2}$  and  $2p_{1/2}2p_{3/2}^43s_{1/2}$  which stabilize its energy relative to the ground state. However, due to the

second configuration where  $2p_{3/2}$  is quadruply occupied, the energy of  $1^\circ(1)$  does not lower as dramatically as that of  $2^\circ$ . In particular, the  $1^\circ(1)$  energy never falls below the ground state energy. As  $c$  approaches then passes  $c_0/14$ ,  $3s_{1/2}$  crosses below  $2p_{3/2}$  and  $1^\circ(1)$  destabilizes relative to  $0^e$ . The rate of destabilization is reduced as  $c$  approach  $c^*$  due to the appearance of the configuration  $2p_{1/2}^2 2p_{3/2} 3s_{1/2}^2 4s_{1/2}$  in the expansion of  $1^\circ(1)$ .

The last odd-parity state included in our discussion is  $0^\circ$  (nominally  $^2[1/2]_0^o$ ) which, for  $c_0/10 \lesssim c \leq c_0$  comprises mainly of  $2p_{1/2} 2p_{3/2}^4 3s_{1/2}$  which, similarly to the case of  $1^\circ(2)$ , causes  $0^\circ$  to destabilize relative to the nominal ground state. However, unlike  $1^\circ(2)$ , the absence of the configuration  $1^\circ(2)$  in the expansion of  $0^\circ$  means that its energy continues to rise until  $c \approx c_0/10$ , where an avoided crossing with higher (nominally)  $^2[1/2]_0^o$  state (not shown) changes the configuration of  $0^\circ$  to  $2p_{1/2}^2 2p_{3/2}^3 3d_{5/2}$ . Since the  $3d_{5/2}$  orbital destabilizes with decreasing  $c$  at a much slower rate than  $2p_{3/2}$ , the  $0^\circ$  energy experiences a steep downturn relative to the ground state energy for  $c \lesssim c_0/10$ .

Next, we consider the even-parity excited states  $1^e$  and  $2^e$ , which correspond to  $^2[1/2]_1$  and  $^2[5/2]_2$  at  $c = c_0$ . These states both start out at as combinations of  $2p_{1/2}^2 2p_{3/2}^3 3p_{1/2}$  and  $2p_{1/2}^2 2p_{3/2}^3 3p_{3/2}$ . As  $c$  is reduced, the  $3p_{1/2}$  energy decreases and the  $3p_{3/2}$  increases at a much slower rate than that of  $2p_{1/2}$ . As a result, the states  $1^e$  and  $2^e$  generally destabilize with respect to the nominal ground state  $0^e$ . However, the stabilization pattern of  $2^e$  display a peculiar feature. At  $c \approx c_0/13$ , the configuration  $2p_{1/2}^2 2p_{3/2}^3 3p_{3/2}$  is replaced by  $2p_{1/2}^2 2p_{3/2}^2 3s_{1/2}^2$  from the CI expansion of  $1^e$  and  $2^e$ . As a result, the decrease of the  $2^e$  energy becomes even more precipitous and at  $c \approx c_0/14$ , it becomes less than the  $0^e$  energy, thus making  $2^e$  the new ground state of neon.

Finally, we consider the state  $3^e$ , which is labeled  $^2[5/2]_3$  at  $c = c_0$ . The dominant configuration in state remains  $2p_{1/2}^2 2p_{3/2}^3 3p_{3/2}$  for all  $c^* \lesssim c \leq c_0$ . As a result, it destabilizes continuously relative to the ground state, albeit not rapidly enough for it to cross the nominal ground state anywhere in the interval  $c^* \lesssim c \leq c_0$ .

#### Appendix D: Results for molecules

In the relativistic picture, the states of atoms and molecules are described by four-component Dirac spinors  $\psi = (\psi_L^\alpha, \psi_L^\beta, \psi_S^\alpha, \psi_S^\beta)^\top$ , where L and S indicate the large and small components, respectively, while  $\alpha$  and  $\beta$  describe the spin degrees of freedom. The spinor components are, in general, complex numbers so a general collection of four such components has eight degrees of freedom. However, since the spatial and spin degrees of freedom are coupled, the symmetry of the Dirac spinors is described by the double groups, where the total spinor transforms under fermion irreducible representations spanned by half-integer spin functions [12]. Fur-

thermore, the real and imaginary parts of each spinor component are spanned by boson irreducible representations, which are irreducible representations of conventional single point groups. Therefore, each spinor component can be described by scalar functions, or orbitals.

The symmetries of the ammonia and water molecules are described by the  $C_{3v}$  and  $C_{2v}$  double groups. For example, exploiting the symmetry of the Dirac Hamiltonian, it can be shown that in the  $C_{2v}$  double group, the real and imaginary parts of the large component transform under the  $(a_1, a_2)$  and  $(b_1, b_2)$  boson irreducible representations for  $\psi_L^\alpha$  and  $\psi_L^\beta$ , correspondingly [35]. At the nominal  $c$ , molecular orbitals of ammonia and water are spanned only by a real or imaginary part of a single component, neglecting vanishing contribution from other components. Therefore, these orbitals are described by a single irreducible representation, in compliance with results from non-relativistic calculations. At decreased  $c$ , however, the molecular orbitals are spanned by multiple real and imaginary parts of the spinor components and one can no longer assign a single irreducible representation to molecular orbitals. For this reason, the symmetry labels in the MO diagrams of ammonia and water are presented only at the nominal speed of light, but not for smaller  $c$ .

In the MO diagram for water (Fig. 4 in the main text), the  $\sigma$  and  $\sigma^*$  linear combinations of  $1s$  orbitals of two hydrogen atoms have the  $a_1$  and  $b_2$  symmetries. For oxygen at the nominal  $c$ , the atomic orbitals  $2s_{1/2}$  and  $3s_{1/2}$  have the symmetry of  $a_1$  whereas the  $2p$  orbitals have the symmetries of  $a_1$ ,  $b_2$ , and  $b_1$ . In the ammonia MO diagram (Fig. 6 in the main text), the three linear combinations  $\psi_1$ ,  $\psi_2$ , and  $\psi_3$  of  $1s$  orbitals belonging to the three hydrogen atoms have  $a_1$  and doubly degenerate  $e$  symmetries. At the nominal  $c$ , the  $2s_{1/2}$  and  $3s_{1/2}$  atomic orbitals of nitrogen have symmetry  $a_1$  whereas the  $2p$  orbitals have symmetries  $a_1$  and  $e$ . In atomic calculations of oxygen and nitrogen, the  $3s_{1/2}$  spinor was included in the average-of-configuration Dirac-Hartree-Fock method to assess the effect of stabilizing higher lying spinors on molecular bonding. For clearer comparison of diagrams, we keep the energy unit constant and equal to that at the nominal  $c$ . To better demonstrate the changes in the electronic structure of molecules at the decreased speeds of light, we calculated the radial density distribution in DIRAC19 [12, 13] for each molecular orbital of water and ammonia as

$$\rho(r) = \int_0^{2\pi} \int_0^\pi \rho(\mathbf{r}) r^2 \sin \theta d\theta d\phi, \quad (\text{D1})$$

where  $\rho(\mathbf{r}) \equiv |\Psi(\mathbf{r})|^2$  is the electron density and  $\Psi(\mathbf{r})$  is the MO wave function.

The Walsh correlation diagrams for ammonia are shown in Fig. 17. At the nominal and intermediate  $c$ , the minima of the sum of orbital energies correspond to the trigonal pyramidal molecular geometries. For even lower  $c$ , the HOMO stabilization at large angles dominates the

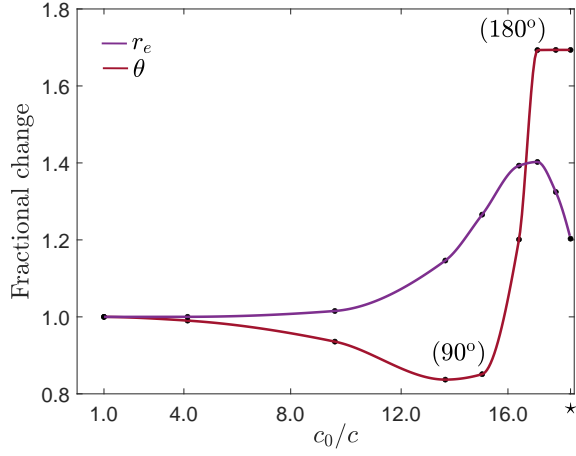


FIG. 13. Fractional changes in the bond distance  $r$  and the bond angle  $\theta$  in the water molecule at different values of the speed of light,  $c$ . The critical value of  $c$  is marked with  $\star$  on the  $x$ -axis,  $c_0/c_0^* = 18.4$ .

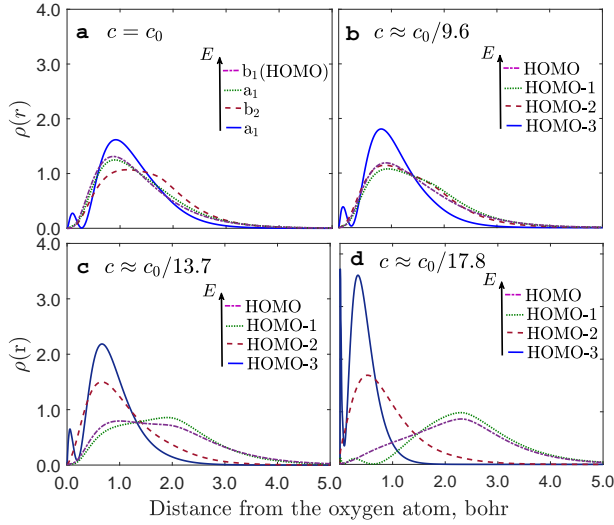


FIG. 14. Radial density distributions for four occupied molecular orbitals of water at different values of the speed of light, (a)  $c = c_0$ , (b)  $c \approx c_0/9.6$ , (c)  $c \approx c_0/13.7$ , and (d)  $c \approx c_0/17.8$ . The oxygen atom is placed at the coordinate origin. The molecular orbitals are labeled in the order of increasing energy. The dark blue solid curve shows the distribution for the lowest occupied molecular orbital, HOMO-3 (HOMO stands for the highest occupied molecular orbital); the dark red dashed curve - HOMO-2; the dark green dotted curve - HOMO-1; and the magenta dot-dashed curve - HOMO. For better resolution, the distance from the oxygen atom is given in the units of the unscaled nominal Bohr radius.

energy changes of other molecular orbitals, leading to the planar molecular geometry.

- [1] Uzan, J.-P. Varying constants, gravitation and cosmology. *Living Rev. Relativ* **14**, 1–155 (2011). URL <https://doi.org/10.12942/lrr-2011-2>.
- [2] Safronova, M. S. *et al.* Search for new physics with atoms

and molecules. *Rev. Mod. Phys.* **90**, 025008 (2018). URL <https://doi/10.1103/RevModPhys.90.025008>.

- [3] Flambaum, V. V. & Dzuba, V. A. Search for variation of the fundamental constants in atomic, molecular, and

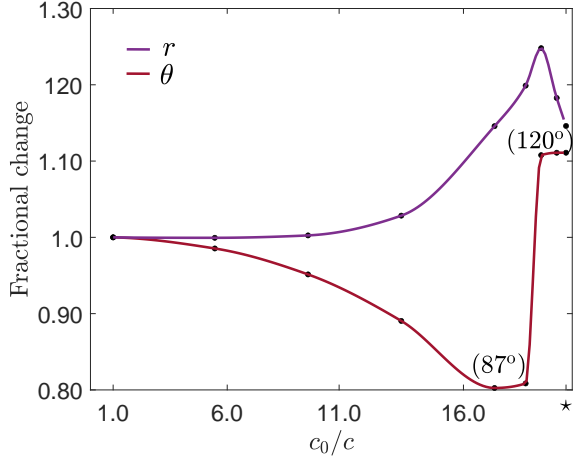


FIG. 15. Fractional changes in the bond distance  $r$  and the bond angle  $\theta$  in the ammonia molecule at different values of the speed of light,  $c$ . The critical value of  $c$  is marked with  $\star$  on the  $x$ -axis,  $c_0/c_N^* = 20.9$ .

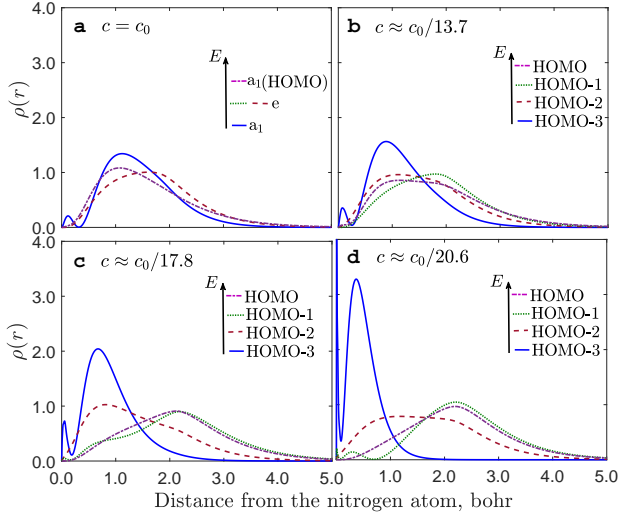


FIG. 16. Radial density distributions for four occupied molecular orbitals of ammonia at different values of the speed of light, (a)  $c = c_0$ , (b)  $c \approx c_0/13.7$ , (c)  $c \approx c_0/17.8$ , and (d)  $c \approx c_0/20.6$ . The nitrogen atom is placed at the coordinate origin. The molecular orbitals are labeled in the order of increasing energy. The dark blue solid curve shows the distribution for the lowest occupied molecular orbital, HOMO-3 (HOMO stands for the highest occupied molecular orbital); the dark red dashed curve - HOMO-2; the dark green dotted curve - HOMO-1; and the magenta dot-dashed curve - HOMO. For better resolution, the distance from the nitrogen atom is given in the units of the unscaled nominal Bohr radius.

nuclear spectra. *Can. J. Phys.* **87**, 25–33 (2009). URL <https://doi.org/10.1139/p08-072>.

- [4] Pašteka, L. F., Hao, Y., Borschevsky, A., Flambaum, V. V. & Schwerdtfeger, P. Material size dependence on fundamental constants. *Phys. Rev. Lett.* **122**, 160801 (2019). URL <https://doi.org/10.1103/PhysRevLett.122.160801>.

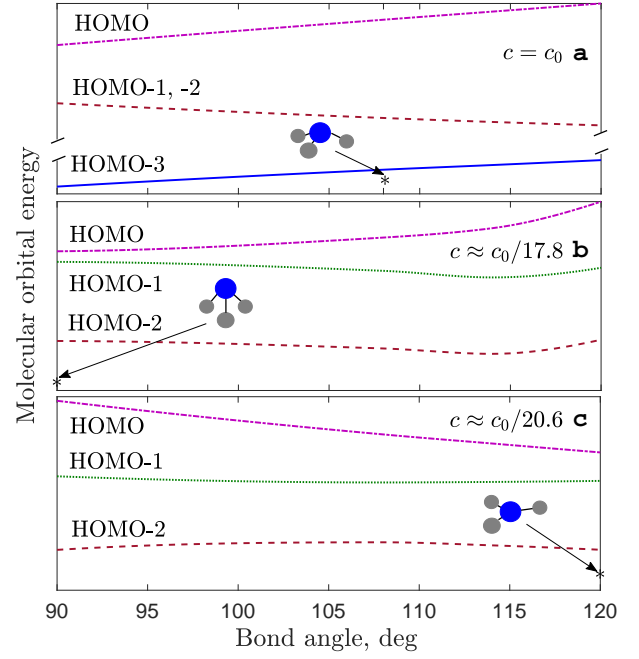


FIG. 17. Walsh correlation diagrams of ammonia showing the energies of four valence molecular orbitals as functions of bond angle at different speeds of light, (a)  $c = c_0$ , (b)  $c \approx c_0/17.8$ , and (c)  $c \approx c_0/20.6$ . In panels b and c, the lowest occupied molecular orbital is omitted as it reduces to  $2s_{1/2}$  core spin-orbital of nitrogen and does not participate in the formation of nitrogen-hydrogen bonds. The energies of molecular orbitals at the equilibrium bond angles correspond to those in Fig. 6 in the main text.

160801.

- [5] Webb, J. K. *et al.* Indications of a spatial variation of the fine structure constant. *Phys. Rev. Lett.* **107**, 191101 (2011). URL <https://doi.org/10.1103/PhysRevLett.107.191101>.
- [6] Derevianko, A. & Pospelov, M. Hunting for topological dark matter with atomic clocks. *Nat. Phys.* **10**, 933–936 (2014). URL <https://doi.org/10.1038/nphys3137>.
- [7] Carter, B. Large number coincidences and the anthropic principle in cosmology. In *Confrontation of cosmological theories with observational data*, 291–298 (Springer, 1974).
- [8] Carr, B. J. & Rees, M. J. The anthropic principle and the structure of the physical world. *Nature* **278**, 605–612 (1979). URL <https://doi.org/10.1038/278605a0>.
- [9] Dubillard, S., Rota, J.-B., Saue, T. & Fægri, K. Bonding analysis using localized relativistic orbitals: Water, the ultrarelativistic case and the heavy homologues  $H_2X$  ( $X=Te, Po, eka-Po$ ). *J. Chem. Phys.* **124**, 154307 (2006). URL <https://doi.org/10.1063/1.2187001>.
- [10] Dyall, K. G. & Fægri, K. J. *Introduction to Relativistic Quantum Chemistry* (Oxford University Press, 2007).
- [11] Reiher, M. & Wolf, A. *Relativistic Quantum Chemistry* (Wiley-VCH, 2015), 2nd edn.
- [12] Saue, T. & Jensen, H. J. A. Quaternion symmetry in relativistic molecular calculations: The Dirac–Hartree–Fock method. *J. Chem. Phys.* **111**, 6211–6222 (1999). URL <https://doi.org/10.1063/1.479958>.

- [13] Saue, T. *et al.* The DIRAC code for relativistic molecular calculations. *J. Chem. Phys.* **152**, 204104 (2020). URL <https://doi.org/10.1063/5.0004844>.
- [14] Greiner, W. *Relativistic Quantum Mechanics: Wave Equations* (Springer-Verlag Berlin Heidelberg, 2000).
- [15] Zeldovich, Y. B. & Popov, V. S. Electronic Structure of Superheavy Atoms. *Sov. Phys. Uspekhi* **14**, 673–694 (1972). URL <https://doi.org/10.1070/pu1972v014n06abeh004735>.
- [16] Greiner, W. & Reinhardt, J. *Quantum Electrodynamics* (Springer Berlin Heidelberg, 2008).
- [17] Friedrich, H. & Friedrich, H. *Theoretical atomic physics*, vol. 4 (Springer, Cham, 2017).
- [18] Gamow, G. *Mr. Tompkins in Wonderland; or, Stories of  $c$ ,  $G$ , and  $h$*  (The Macmillan Company, New York, 1940).
- [19] NIST Atomic Spectra Database. URL [http://physics.nist.gov/cgi-bin/AtData/main\\_asd](http://physics.nist.gov/cgi-bin/AtData/main_asd).
- [20] Benner, S. A., Ricardo, A. & Carrigan, M. A. Is there a common chemical model for life in the universe? *Curr. Opin. Chem. Biol.* **8**, 672–689 (2004). URL <https://doi.org/10.1016/j.cbpa.2004.10.003>.
- [21] Christensen, H. N. Role of amino acid transport and countertransport in nutrition and metabolism. *Physiol. Rev.* **70**, 43–77 (1990). URL <https://doi.org/10.1152/physrev.1990.70.1.43>.
- [22] Engel, T. & Reid, P. *Physical Chemistry* (Pearson Education, Inc., 2012).
- [23] Chang, R. *Physical Chemistry for the Biosciences* (University Science Books, 2005), 1st edn.
- [24] Stillinger, F. H. Water revisited. *Science* **209**, 451–457 (1980). URL <https://www.science.org/doi/abs/10.1126/science.209.4455.451>.
- [25] Roberts, B. M. *et al.* Search for domain wall dark matter with atomic clocks on board global positioning system satellites. *Nature Comm.* **8**, 1195 (2017). URL <http://www.nature.com/articles/s41467-017-01440-4>.
- [26] Flambaum, V. V. & Kozlov, M. G. Limit on the cosmological variation of  $m_p/m_e$  from the inversion spectrum of ammonia. *Phys. Rev. Lett.* **98**, 240801 (2007). URL <https://doi/10.1103/PhysRevLett.98.240801>.
- [27] Tiesinga, E., Mohr, P. J., Newell, D. B. & Taylor, B. N. The 2018 CODATA Recommended Values of the Fundamental Physical Constants. Tech. Rep., National Institute of Standards and Technology (2020). URL <http://physics.nist.gov/constants>.
- [28] Johnson, W. *Atomic Structure Theory: Lectures on Atomic Physics* (Springer-Verlag Berlin Heidelberg, 2007).
- [29] Johnson, W. & Soff, G. The Lamb shift in hydrogen-like atoms,  $1 \leq Z \leq 110$ . *At. Data Nucl. Data Tables* **33**, 405–446 (1985). URL <https://www.sciencedirect.com/science/article/pii/0092640X85900105>.
- [30] Ferreira, E. M. & Sesma, J. Zeros of the Macdonald function of complex order. *J. Comput. Appl. Math.* **211**, 223–231 (2008). URL <https://www.sciencedirect.com/science/article/pii/S0377042706007084>.
- [31] Brown, G. E., Ravenhall, D. G. & Peierls, R. E. On the interaction of two electrons. *Proc. R. Soc. Lond. A* **208**, 552–559 (1951). URL <https://royalsocietypublishing.org/doi/abs/10.1098/rspa.1951.0181>.
- [32] Sapirstein, J. Theoretical methods for the relativistic atomic many-body problem. *Rev. Mod. Phys.* **70**, 55–76 (1998). URL <https://doi/10.1103/RevModPhys.70.55>.
- [33] Barysz, M. & Ishikawa, Y. *Relativistic methods for chemists* (Springer, Dordrecht, 2010).
- [34] Dzuba, V. A., Flambaum, V. V. & Webb, J. K. Calculations of the relativistic effects in many-electron atoms and space-time variation of fundamental constants. *Phys. Rev. A* **59**, 230–237 (1999). URL <https://doi/10.1103/PhysRevA.59.230>.
- [35] Bast, R. *et al.* DIRAC21 (2021). URL <https://doi.org/10.5281/zenodo.4836496>.